Physica Scripta

PAPER

RECEIVED
26 August 2025

REVISED
11 December 2025

ACCEPTED FOR PUBLICATION
24 December 2025

PUBLISHED
6 January 2026

First-principles study of electronic, magnetic, and mechanical properties in pristine and 3D-metal intercalated titanium dichalcogenides TiX_2 and $YTiX_2$ (X = S, Se, Te; Y = Cr, Mn, Fe)

Dj Guendouz[1,2], **H Baaziz**[2,3,*], **T Ghellab**[2,3] **and Z Charifi**[2,3,*]

[1] Physics Department, High Normal School of Bousaada , Algeria
[2] Laboratory of physics and chemistry of materials, University of M'sila , Algeria
[3] Department of Physics, Faculty of Science, University of M'sila, 28000 M'sila, Algeria
[*] Authors to whom any correspondence should be addressed.

E-mail: zoulikha.charifi@univ-msila.dz **and** charifizoulikha@gmail.com

Keywords: titanium dichalcogenides, Van der Waals gap, magnetic intercalation, elastic anisotropy, half-metallicity

Abstract

This work presents a comprehensive first-principles investigation of the structural, electronic, magnetic, and mechanical properties of the layered titanium dichalcogenides TiX_2 (X = S, Se, Te) and their magnetically intercalated variants $YTiX_2$ (Y = Cr, Mn, Fe). All compounds are found to crystallize in the hexagonal 1T-CdI_2 structure (space group P $\bar{3}$ m1), with intercalation occurring at the octahedral site within the van der Waals gap. Our calculations reveal that while the parent TiX_2 compounds are non-magnetic semiconductors (TiS_2) or metals ($TiSe_2$, $TiTe_2$), intercalation induces a transition to ferromagnetic metallic ($CrTiX_2$, $MnTiSe_2$, $MnTiTe_2$, and $FeTiTe_2$) or half-metallic ($MnTiS_2$, $FeTiS_2$, and $FeTiSe_2$) states, the latter exhibiting 100% spin polarization at the Fermi level —a coveted property for spintronics. Magnetic moment analysis reveals complex interplay between localized moments on the intercalants and induced antiparallel moments on Ti atoms, mediated by strong superexchange coupling. Mechanically, all compounds are stable and exhibit significant anisotropy, which is visually confirmed by 3D representations of elastic moduli. The pristine compounds show classic layer-driven anisotropy ($C_{11} > C_{33}$), which is often inverted ($C_{33} > C_{11}$) upon intercalation due to a covalent 'pillaring' effect. Pugh's and Poisson's ratios classify most compounds as brittle with mixed ionic-covalent bonding, with notable exceptions like $FeTiSe_2$ and $MnTiTe_2$ showing a ductile character. This study provides a calculated foundation for experimental work by establishing the elastic stability, predicting structural parameters, and identifying the promising half-metallic ferromagnetism in $MnTiS_2$ and $FeTiS_2$, thereby guiding the targeted synthesis and characterization of these materials for spintronic applications.

1. Introduction

The pursuit of advanced functional materials has intensified research on transition metal dichalcogenides (TMDs) and their intercalation compounds, driven by their exceptional properties relevant to spintronics, quantum information processing, and solid-state thermoelectrics [1–3]. Within this class, the titanium dichalcogenide series TiX_2 (X = S, Se, Te) serves as a foundational system, crystallizing in the canonical 1T-CdI_2 prototype structure. This layered architecture features a plane of titanium atoms octahedrally coordinated by two closed-packed chalcogen layers, facilitating anisotropic physical properties and enabling host–guest chemistry via intercalation.

A longstanding and critical debate surrounds the fundamental electronic nature of the pristine TiX_2 compounds. Titanium diselenide ($TiSe_2$) exhibits a charge density wave (CDW) transition below ~220 K [4], which is often linked to its contested electronic ground state, described variably as semiconducting [5, 6] or semimetallic [7]. In contrast, TiS_2 shows no CDW instability, yet its electronic character is similarly disputed. While

early angle-resolved ultraviolet photoelectron spectroscopy (ARUPS) [8–11], pressure-dependent Hall measurements [12, 13], and theoretical studies [14] suggested a small-gap semiconductor scenario, subsequent work challenges this view. Titanium ditelluride ($TiTe_2$) remains the least controversial, consistently identified as a semimetal with a significant band overlap [15]. Several theoretical studies have sought to determine the electronic nature of TiS_2 and $TiSe_2$, particularly regarding the existence and size of an energy band gap. Early work by Peter Krusius [16], employing the self-consistent OPW method [17, 18], proposed TiS_2 to be a semiconductor. However, no definitive conclusion was drawn on the energy band gap for the $TiSe_2$ compound [19]. Subsequent studies using the OPW method by Umrigar *et al* [20] found a band gap of 0.5 eV for TiS_2. In contrast, Lemoigno *et al* [21] later investigated the electronic structure of TiS_2 through a combined analysis of theoretical and experimental spectra, arguing for a semimetallic state. Von Boehm *et al* [22] analyzed the valence one-electron densities of $TiSe_2$ using the self-consistent orthogonalized-plane wave (SCOPW) method. Clerc *et al* [23] conducted a theoretical study on TiS_2, showing that the calculated energy bands agreed with prior data. Fang *et al* [24] analyzed the electronic structure of 1T-TiS_2 and 1T-$TiSe_2$ using the localized spherical wave (LSW) method, finding them to be semimetallic. This ongoing debate in the literature underscores the sensitivity of the electronic structure to the chosen computational methodology and highlights the complexity that our current study on pristine and intercalated TiX_2 aims to address in its own context. Directly contradicting this, Allan *et al* combined high-pressure X-ray diffraction with pseudopotential calculations to identify an isostructural semiconductor-to-semimetal transition in TiS_2 at ∼4 GPa, implying a semiconducting state at ambient pressure that closes under compression [25]. The most recent work by Liu *et al* [26], integrating *in situ* transport measurements with first-principles calculations, firmly supports a semimetallic ground state for TiS_2 that is robust under high pressure, further underscoring the lack of consensus.

Parallel to these fundamental studies, applied research has explored the functionalization of these materials, particularly through the intercalation of 3d transition metals (Y) into the van der Waals gap of TiS_2 to form $YTiS_2$. These compounds are promising electrode materials [27], with their electronic structure tunable by the choice of chalcogen, as the bond character evolves from more ionic (TiS_2) to more covalent ($TiTe_2$) [28, 29]. The structural evolution under pressure is also key, with 1T-$TiTe_2$ undergoing a phase transition to a monoclinic (C2/m) phase above 8 GPa [30]. The chemical bonding in intercalated compounds (Y = Cr, Fe) has been probed via molecular orbital theory [31], while their electronic structures have been characterized by a suite of spectroscopic techniques (XPS, ARPES, ARIPES) and magnetization studies [32, 33]. Theoretical investigations, including full-potential linearized augmented plane wave (FP-LAPW) [34] and pseudopotential [35] methods, have confirmed the metallic character of certain intercalated compounds, evidenced by states at the Fermi level. However, a systematic first-principles study encompassing the complete $YTiX_2$ series is absent from the literature. The specific comparative analysis of TiS_2 and $FeTiS_2$ by Vanadan [36] underscores the profound electronic restructuring that intercalation can induce, yet it also highlights the need for a more comprehensive exploration across the entire chemical space.

This literature survey thus identifies two pivotal unresolved challenges: (*i*) the enduring controversy over the fundamental electronic ground state (semiconducting versus metallic) of the pristine TiX_2 compounds, and (*ii*) the lack of a unified computational framework that concurrently evaluates the role of both the intercalant (Y) and the host chalcogen (X) on the structural stability, electronic structure, and magnetic properties of the $YTiX_2$ series.

To resolve these critical gaps, we undertake a comprehensive density functional theory (DFT) investigation of both the pristine TiX_2 and intercalated $YTiX_2$ systems (X = S, Se, Te; Y = Cr, Mn, Fe). This work is designed to decisively clarify the electronic nature of the pristine hosts and establish predictive design principles for property optimization through intercalation engineering. We achieve this by rigorously evaluating the thermodynamic stability and conducting a detailed analysis of the electronic structures—including band dispersions and density of states—and magnetic configurations across all compounds. Our computational methodology is elaborated in section II. The results are presented and discussed in section 3, organized to sequentially examine structural stability (3.1), electronic and magnetic properties (3.2), and mechanical behavior (3.3). This systematic approach provides a holistic understanding of how the synergistic effects of Y and X govern material functionality, thereby offering a roadmap for the targeted development of these materials.

2. Computational approach and details

First-principles calculations were conducted based on density functional theory (DFT) using the full-potential linearized augmented plane wave (FP-LAPW) method, implemented in the WIEN2k computational package [37]. This method provides a highly accurate, all-electron approach that makes no shape approximation to the potential or charge density.

Table 1. The atomic positions of TiX_2 (X = S, Se and Te) and $YTiX_2$ (Y = Cr, Mn and Fe, X = S, Se and Te) compounds.

Compounds	Atom	Wyckoff Position	Coordinates
TiX_2	Ti	1a	(0.0.0)
P $\bar{3}$ m1 (No. 164)	X	2d	(1/3, 2/3, 1/4), (2/3, 1/3, 3/4)
$YTiX_2$	Y	1b	(0, 0, 0.5)
P $\bar{3}$ m1-(No. 164)	Ti	1a	(0.0.0)
	X	2d	(1/3, 2/3, 1/4), (2/3, 1/3, 3/4)

To treat electron exchange and correlation effects, we employed two prevalent approximations: the local density approximation (LDA) and the generalized gradient approximation (GGA) in the parameterization of Perdew, Burke, and Ernzerhof (PBE) [38]. Furthermore, to achieve a more accurate description of electronic properties, particularly for determining band gaps and related characteristics, we additionally applied the Engel-Vosko (EV-GGA) functional [39], which is designed to better reproduce exchange–correlation potentials.

The atomic spheres were defined by carefully chosen muffin-tin radii. Inside these non-overlapping spheres, the valence wave functions were expanded in spherical harmonics up to a maximum angular momentum of $l_{max} = 10$. In the interstitial region between these spheres, the basis set consisted of plane waves, with the charge density Fourier expansion truncated at $G_{max} = 12$. The convergence of the basis set was rigorously controlled by the parameter $R_{MT} \times K_{max} = 9$, where R_{MT} is the smallest muffin-tin radius and K_{max} is the magnitude of the largest K-vector in the plane wave expansion. The potential was expanded as a Fourier series with a higher cutoff of $G_{max} = 12$ to ensure a precise representation.

Structural properties were determined by optimizing the total energy with respect to the unit cell volume. A series of calculations were performed for different volumes, and the resulting energy-volume data points were fitted to the Murnaghan equation of state [40]. This fitting procedure yielded the equilibrium lattice parameters, the equilibrium volume V_0, the bulk modulus B_0, and its pressure derivative B' for each compound. An energy convergence threshold of 0.1 mRy between successive self-consistent field (SCF) cycles was used for all calculations to ensure high numerical accuracy.

It is important to note that the standard LDA and GGA functionals employed in this study do not explicitly account for long-range van der Waals (vdW) interactions. These forces are crucial for accurately describing the binding between the layered X-Ti-X slabs. Our choice of functional was guided by the primary aim of this work: to consistently survey the electronic, magnetic, and in-plane mechanical properties across the entire series of compounds, which are dominated by strong covalent intra-layer bonding. While this approach may lead to an overestimation of the *c*-lattice parameter and an underestimation of the interlayer binding energy, it is expected to have a minimal impact on the qualitative trends of the key properties under investigation, such as band gaps, magnetic moments, and in-plane elastic constants.

3. Results and discussions

3.1. Structural properties

The transition metal dichalcogenides (TMDs) form a vast family of layered compounds with the formula MX_2, where M is a transition metal (such as Mo, W, Zr, or Ti) and X is a chalcogen (S, Se, or Te). This work focuses on the titanium-based systems TiX_2 and their magnetically intercalated variants $YTiX_2$. All compounds crystallize in the 1T-polytype, adopting the CdI_2 structure with the hexagonal space group P$\bar{3}$m1 (No. 164).

The specific Wyckoff positions and atomic coordinates for all structures are summarized in table 1. In the parent TiX_2 structure, each Ti atom is octahedrally coordinated by six X atoms, forming robust X–Ti–X sandwich layers. These covalent trilayers are stacked along the *c*-axis and separated by a van der Waals gap. Intercalation of magnetic guest atoms Y (Cr, Mn, Fe) into this gap yields the $YTiX_2$ compounds, which retain the overall P$\bar{3}$m1 symmetry, as illustrated in figure 1. While the interlayer interaction remains van der Waals-like, the intercalated Y atoms form strong covalent-ionic bonds within the octahedral coordination environment, creating a 'pillaring' effect that modifies the mechanical properties while maintaining the layered character necessary for potential exfoliation.

A critical aspect of this study was to determine not only the ground-state structure but also the favorable magnetic state for each compound. To achieve this, we performed first-principles total energy calculations as a function of unit cell volume for both non-magnetic (NM) and ferromagnetic (FM) configurations. Figures 2(a) and (b) exemplifies this procedure, showing the characteristic energy-volume curves for TiS_2 and $CrTiS_2$. From these calculations, a key finding emerges: the NM state is energetically favorable for the parent TiX_2 compounds. In contrast, the intercalated compounds are known to crystallize into a hexagonal magnetic phase at

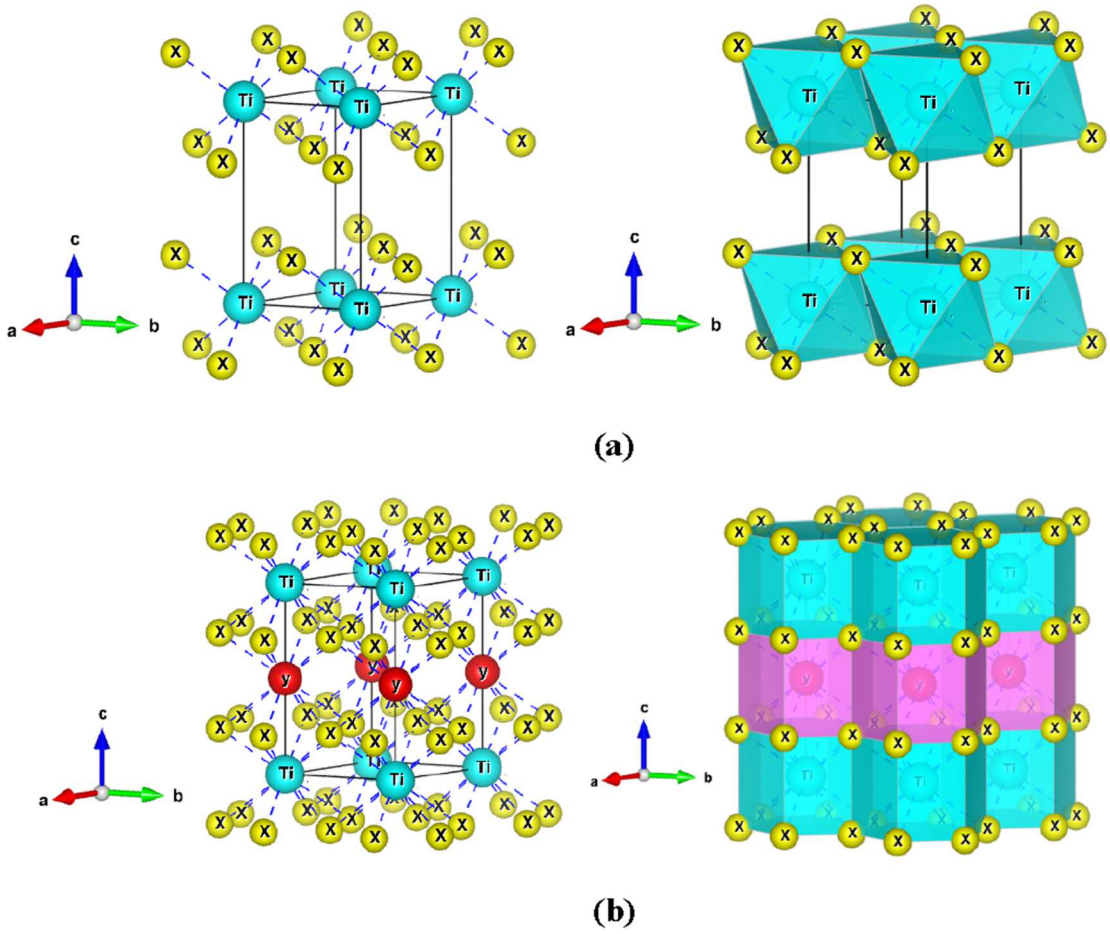

Figure 1. Crystal structures of (a) pristine TiX_2 and (b) intercalated $YTiX_2$ (X = S, Se, Te; Y = Cr, Mn, Fe). Left panels: ball-and-stick models. Right panels: polyhedral representations. In (a), the empty region between layers is the van der Waals (vdW) gap. In (b), the Y atoms (purple) occupy octahedral sites within this gap, where they form strong chemical bonds with the chalcogen framework, as unambiguously shown by their octahedral coordination polyhedra.

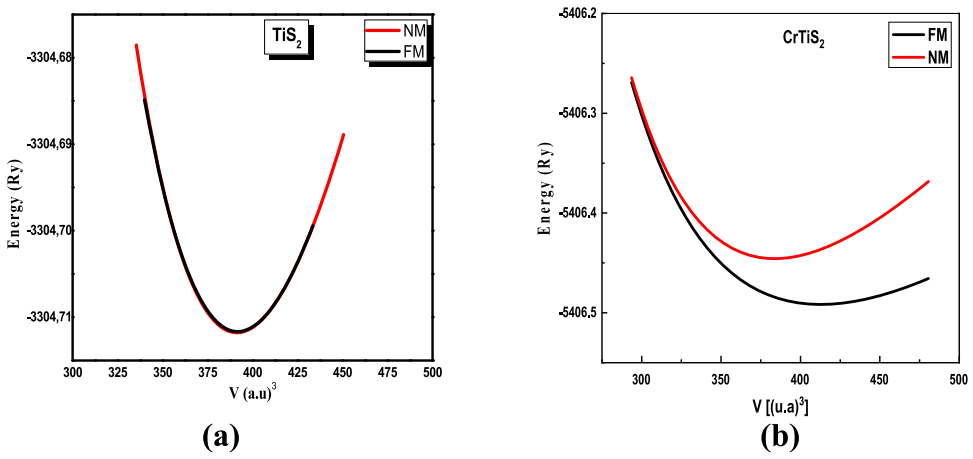

Figure 2. Variation of total energies as a function of volume of unit cell for using GGA for TiS_2 and $CrTiS_2$.

low temperatures; our calculations confirm that a FM description is necessary to accurately capture their ground-state properties.

The equilibrium structural parameters—lattice constants (a, c), bulk modulus (B), and its pressure derivative (B')—extracted from these calculations are comprehensively listed in table 2 for both the LDA and GGA approximations. The well-known systematic error of these functionals is clearly observed: GGA consistently overestimates the lattice parameters while LDA underestimates them, a consequence of their treatment of

Table 2. Calculated lattice constants (a and c) in Å, bulk modulus (B) in GPa and pressure derivative (B'), using LDA and GGA compared with the available experimental and theoretical data of TiX_2 (X = S, Se and Te) and $YTiX_2$ (Y = Cr, Mn and Fe, X = S, Se and Te).

Compounds	GGA					LDA				
	a	c	c/a	B	B'	a	c	c/a	B	B'
TiS_2-NM	3.431, 3.407 [24, 41], 3.40 [27], 3.311 [26]	5.752, 5.695 [24, 41], 5.512 [26]	1.676	95.03	4.01	3.353	5.593	1.668	106.82	4.04
$CrTiS_2$-FM	3.484, 3.4395 [35]	5.810, 5.9303 [35]	1.667	91.06	5.00	3.369	5.618	1.667	133.40	5.00
$MnTiS_2$-FM	3.498	5.845	1.670	75.99	5.00	3.361	5.592	1.663	123.63	5.00
$FeTiS_2$-FM	3.457	5.756	1.665	94.89	5.00	3.330	5.564	1.670	136.30	5.00
$TiSe_2$-NM	3.562, 3.540 [24]	6.047, 6.008 [24]	1.697	78.93	4.03	3.470	5.892	1.697	95.56	4.83
$CrTiSe_2$-FM	3.667	6.226	1.697	68.32	5.00	3.486	5.909	1.695	104.11	5.00
$MnTiSe_2$-FM	3.693	6.351	1.719	95.46	4.79	3.519	5.975	1.697	96.30	5.00
$FeTiSe_2$-FM	3.460	5.951	1.719	74.40	5.00	3.468	5.888	1.697	72.35	5.00
$TiTe_2$-NM	3.798, 3.777 [42]	6.522, 6.498 [42]	1.717	60.84	4.05	3.695	6.355	1.719	74.49	4.94
$CrTiTe_2$-FM	3.925	6.751	1.72	51.08	5.00	3.764	6.474	1.719	82.35	5.00
$MnTiTe_2$-FM	3.933	6.747	1.719	64.58	5.00	3.743	6.437	1.719	77.97	5.00
$FeTiTe_2$-FM	3.769	6.461	1.714	103.92	3.64	3.657	6.290	1.719	113.07	5.00

electron exchange and correlation. Despite this, our GGA results show excellent agreement with available experimental and theoretical data for the parent compounds [24, 26, 27, 41, 42], confirming the reliability of our approach. The data reveals compelling chemical trends. It is clearly seen that the lattice parameters increase monotonically from TiS_2 to $TiSe_2$ to $TiTe_2$, a direct result of the increasing ionic radius of the chalcogen atom ($S^{2-} < Se^{2-} < Te^{2-}$). On the other hand, the bulk modulus decreases across the same series, signifying a softening of the crystal lattice as the bonds lengthen and the van der Waals gap widens.

Upon intercalation, the lattice undergoes a continuous and significant expansion due to the gradual occupation of the octahedral holes. As detailed in table 2, the a and c lattice parameters exhibit a systematic increase down the chalcogen series (S → Se → Te) for pristine TiX_2. A further systematic expansion is observed upon intercalation with Cr and Mn, consistent with a 'pillaring' effect where the guest atom pushes the adjacent chalcogen layers apart. This is a direct physical consequence of intercalation and is a similar feature to that remarked for the intercalation of Li atoms into TiS_2 [43]. For the compound $CrTiS_2$, the value we obtained for the equilibrium lattice parameter ($a = 3.484$ Å) is superior to the existing theoretical results, providing a new benchmark that agrees more closely with the overall trend.

The systematic expansion of the lattice upon intercalation, as detailed in table 2, can be directly correlated with the intrinsic properties of the guest atoms. The observed trend in lattice parameters—where for a given chalcogen (X), the unit cell volume typically follows the sequence $CrTiX_2 < MnTiX_2 < FeTiX_2$—aligns with the increasing metallic radii of the intercalants in their high-spin states (Cr < Mn < Fe). This clear correlation underscores that the 'pillaring' effect is not merely a function of occupation but is quantitatively governed by the size of the intercalated ion. Consequently, the resulting structural distortion serves as a primary tuning knob, which in turn dictates the ensuing electronic and magnetic properties discussed in the following sections.

To the best of our knowledge, this study presents the first complete theoretical investigation of the structural properties for the entire series of $YTiX_2$ compounds in the hexagonal phase. The comprehensive data in table 2 establishes a crucial foundation for understanding the interplay between structure, magnetism, and electronic properties in this fascinating class of layered materials.

3.2. Electronic structure, orbital hybridization, and magnetic properties

The quasi-particle band structures and projected density of states (PDOS) for the pristine TiX_2 and intercalated $YTiX_2$ compounds were computed self-consistently using the EV-GGA approximation, with the lattice parameters optimized for equilibrium. The eigenvalues were evaluated along high-symmetry directions in the three-dimensional hexagonal Brillouin zone (figures 3–6). All energy values are referenced to the *Fermi* level, defined by the highest occupied state ($E_F \equiv 0$ eV).

For the 1T-polytype of TiS_2, the fundamental energy gap was found to be indirect. The valence band maximum (VBM) occurs at the Γ point, while the conduction band minimum (CBM) is located along the Γ-M line, near the M point. The calculated indirect gap is $E_g\ \Gamma \rightarrow M = 0.43$ eV. This semiconducting electronic structure arises from the complete filling of the Ti-t_{2g} manifold, with the gap forming between bonding X-p and antibonding Ti- t_{2g} states. This result is consistent with the work of Liu *et al* [26], who also identified an indirect band gap for TiS_2. However, our calculated gap size diverges from the smaller gap reported in [34], a discrepancy commonly attributed to the systematic underestimation of band gaps by semi-local exchange–correlation functionals in DFT, due to electron self-interaction errors and the absence of a derivative discontinuity in

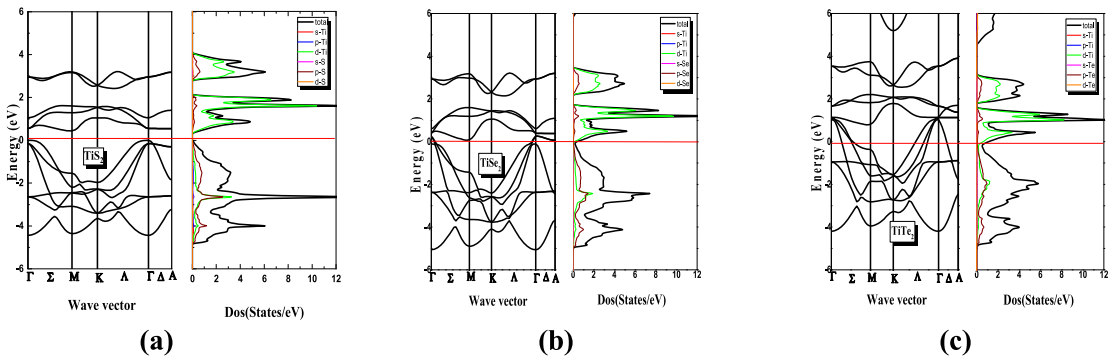

Figure 3. Band structure along the symmetry lines of the Brillouin zone and total and partial density of states for TiX_2(X = S, Se and Te) using EV-GGA.

the exchange–correlation potential. Recent investigations have demonstrated that the electronic and optical properties of TiS_2 are highly dependent on dimensionality. While bulk TiS_2 exhibits semimetallic behavior, monolayer and bilayer TiS_2 display indirect semiconducting characteristics, with computed band gaps of approximately 0.55 eV and 0.42 eV, respectively. Optical absorption analyses further reveal a strong anisotropy and a pronounced redshift with decreasing layer thickness, indicating enhanced light–matter interactions in few-layer structures [44]. These findings underscore the potential of TiS_2-based materials for next-generation nanoelectronic and optoelectronic applications.

In contrast, $TiSe_2$ and $TiTe_2$ exhibit metallic behavior, with bands clearly crossing the Fermi level and a finite density of states ((N(E_F)) at the *Fermi* level. This metallic character is driven by the increasing energy of the chalcogen *p*-orbitals relative to the Ti-*d* orbitals, which enhances *p*-*d* hybridization and leads to the closing of the band gap. This electronic structure aligns with the charge density wave instability observed in $TiSe_2$ [6] and the experimental metallic conductivity in $TiTe_2$ [15].

The intercalation of magnetic 3*d* transition metal atoms (Y = Cr, Mn, Fe) into the van der Waals gap induces strong electronic correlations, spin polarization, and the introduction of additional states within the original TiX_2 gap. In the $CrTiX_2$ series, Cr 3*d* states contribute substantial spectral weight across a wide energy range near E_F. The band structures for both spin channels show a finite density of states at E_F throughout the Brillouin zone, confirming a metallic ground state for all three chalcogenides. The metallic behavior is mainly driven by the partially filled, strongly hybridized Cr-*d* and Ti-*d* t_{2g} bands.

For Mn and Fe intercalates, the electronic structure transitions to a correlated, spin-polarized ground state. The majority-spin channel shows a pronounced band gap (with $\Delta mj = 0.83$ eV for $FeTiS_2$, 0.63 eV for $FeTiSe_2$, and 0.39 eV for $MnTiS_2$), while the minority-spin channel remains metallic with a high N(E_F). The gap in the majority-spin channel results from crystal field splitting of the Y-d orbitals (e.g., Fe-*d* states split into $e_{.g.}$ and t_{2g} manifolds) and exchange interactions, leading to a complete spin polarization of charge carriers at E_F, i.e., $P(E_F) = [N\uparrow(E_F) - N\downarrow(E_F)]/[N\uparrow(E_F) + N\downarrow(E_F)] = 100\%$. This half-metallic property is essential for high-efficiency spintronic devices.

In contrast, for most of the selenide and telluride compounds ($MnTiSe_2$, $MnTiTe_2$, and $FeTiTe_2$), the increased covalency and larger lattice parameters reduce crystal field splitting and on-site Coulomb interactions. This leads to a closing of the gap in both spin channels, confirming a metallic ferromagnetic state, as evidenced by the bands crossing E_F in figures 5 and 6. The persistence of metallicity corresponds to the broader bandwidths associated with the larger chalcogen ions. However, $FeTiSe_2$ is an exception, maintaining a half-metallic state where the majority-spin channel retains a band gap while the minority-spin channel is metallic, similar to the sulfide compounds but with a reduced gap magnitude.

The electronic density of states (DOS) is a crucial tool for understanding material behavior, as it quantifies the available quantum states per unit energy. A high spectral weight at a specific energy level indicates substantial state degeneracy, which influences material properties such as electronic correlations, optical response functions, and charge transport. Our thorough analysis of the total and partial density of states (TDOS/PDOS), computed within the EV-GGA formalism, is instrumental in elucidating the orbital hybridization and bonding characteristics that define the electronic ground state.

For the pristine 1T-TiX_2 compounds, whose TDOS and PDOS are shown in figure 3, the electronic spectrum reveals four distinct regions, categorized by orbital character and bonding nature. The lowest energy region, between −13.0 and −10.0 eV, is dominated by chalcogen *s*-states, representing tightly bound, non-bonding semicore levels with minimal dispersion and limited involvement in covalent bonding. The primary valence band, from −6.0 eV to E_F, arises from strong covalent hybridization between chalcogen *p*-states and Ti

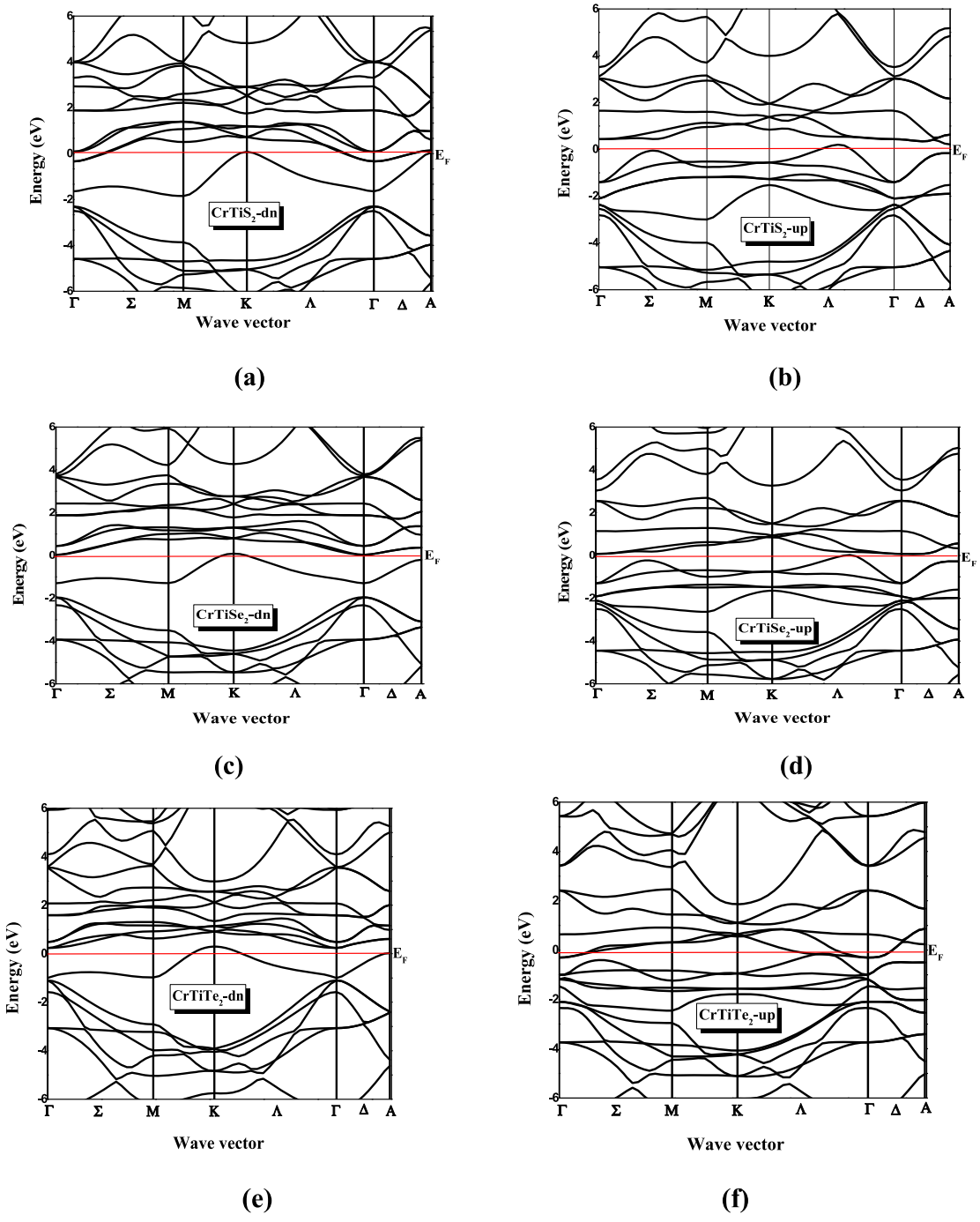

Figure 4. Band structure along the symmetry lines of the Brillouin zone for $CrTiX_2$(X = S, Se and Te) using EV-GGA.

d-states, particularly the t_2g manifold within the octahedral crystal field. The overlap of Ti-*d* and X-*p* PDOS peaks provides clear evidence of this *p*-*d* hybridization, which is key to the structural cohesion of the X-Ti-X layers. Immediately above E_F, the lower conduction band up to approximately 4.0 eV is composed of anti-bonding states formed from the same Ti-*d*–X-*p* hybridization as the valence band. The band gap in TiS_2 results from the energy separation between these bonding and anti-bonding manifolds. The gap gradually closes from S to Se to Te, driven by the increasing energy of the chalcogen *p*-orbitals, which raises the energy of the bonding states and reduces the separation to the anti-bonding states, resulting in the metallic behavior observed in $TiTe_2$. Higher energy conduction states beyond 4.0 eV are primarily Ti $d\ e_g$, s, and *p* states, along with anti-bonding chalcogen *p* and *d* states, consistent with a charge-transfer picture in which X *p*-states form the valence band maximum and Ti *d*-states form the conduction band minimum.

Upon intercalation of magnetic 3*d* transition metal ions (Y = Cr, Mn, Fe) into the octahedral interstitial sites, the electronic structure undergoes significant modification, as demonstrated by the spin-polarized TDOS and PDOS for $YTiX_2$ compounds in figures 7–9. This transformation occurs through two primary

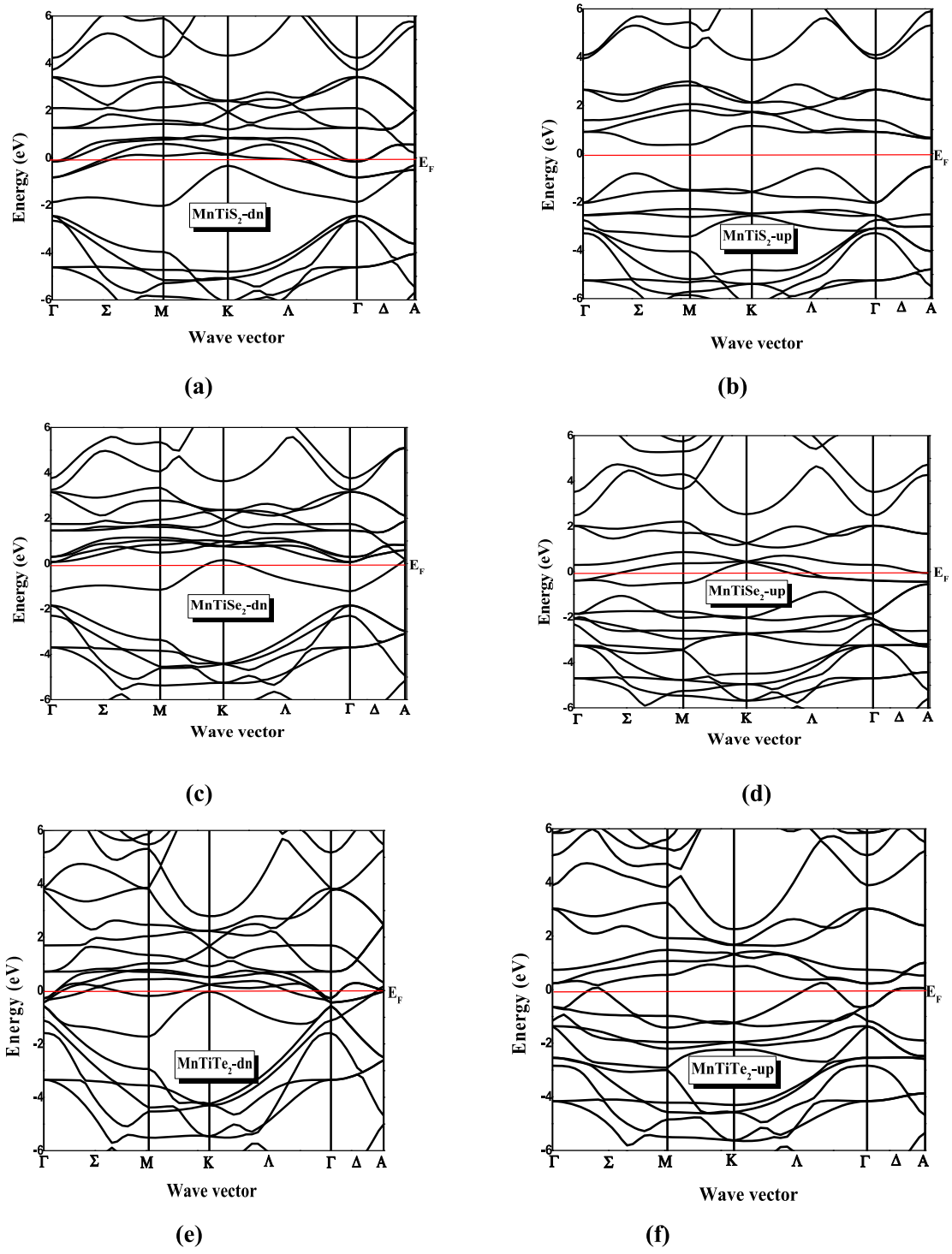

Figure 5. Band structure along the symmetry lines of the Brillouin zone for $MnTiX_2$(X = S,Se and Te) using EV-GGA.

mechanisms: the introduction of new, highly localized *d*-states near E_F and the creation of additional hybridization pathways. The PDOS analysis reveals that the Y *d*-states reside within the original band gap of TiX_2, forming strong hybridizations with both Ti *d*-states and X *p*-states, leading to a new hybridized band complex around E_F. The states near E_F exhibit a mixture of Y-*d*, Ti-*d*, and X-*p* character, indicating a covalent interaction between the guest ion and the host lattice, rather than purely ionic charge donation.

The resulting electronic properties stem directly from the filling and splitting of this hybridized *d*-manifold. The Cr^{3+} (d^3) configuration in $CrTiX_2$ compounds results in partially filled hybridized bands, producing finite DOS at E_F for both spin channels and confirming metallic behavior. In $MnTiS_2$ and $FeTiS_2$, crystal field splitting and strong exchange interactions split the *d*-manifold, such that one spin channel exhibits a gap at E_F while the other remains metallic, creating the half-metallic state with complete spin polarization at E_F. For the

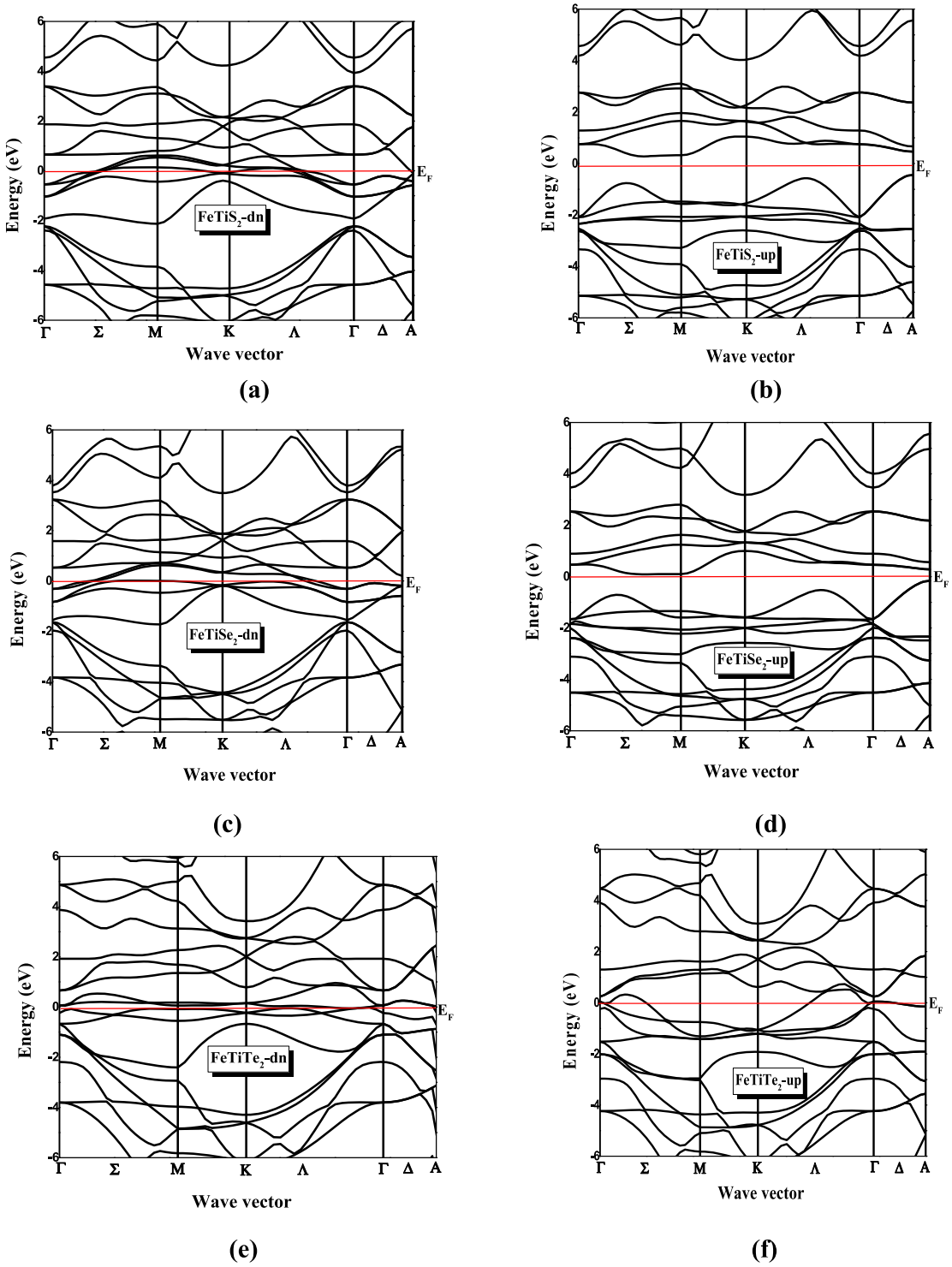

Figure 6. Band structure along the symmetry lines of the Brillouin zone for $FeTiX_2$(X = S, Se and Te) using EV-GGA.

selenide and telluride analogues, increased lattice parameters and enhanced covalency with larger chalcogens reduce crystal field splitting and electron correlation effects, causing narrowing of the *d*-bands and gap closure in both spin channels, which results in metallic ferromagnetism. Throughout all intercalated compounds, while chalcogen *p*-states remain concentrated in the lower valence band, their hybridization with intercalant *d*-states significantly modifies the chemical bonding environment, driving the evolution in electronic and magnetic properties.

The computed magnetic moments for the $YTiX_2$ intercalates, detailed in table 3, provide a nuanced view of their magnetic ground state, revealing insights into hybridization, spin polarization, and the interplay between local and itinerant magnetism. The data unequivocally demonstrates that the net magnetic moment is primarily localized on the intercalant 3*d* ion (Y), as expected. However, the significant, and often antiparallel,

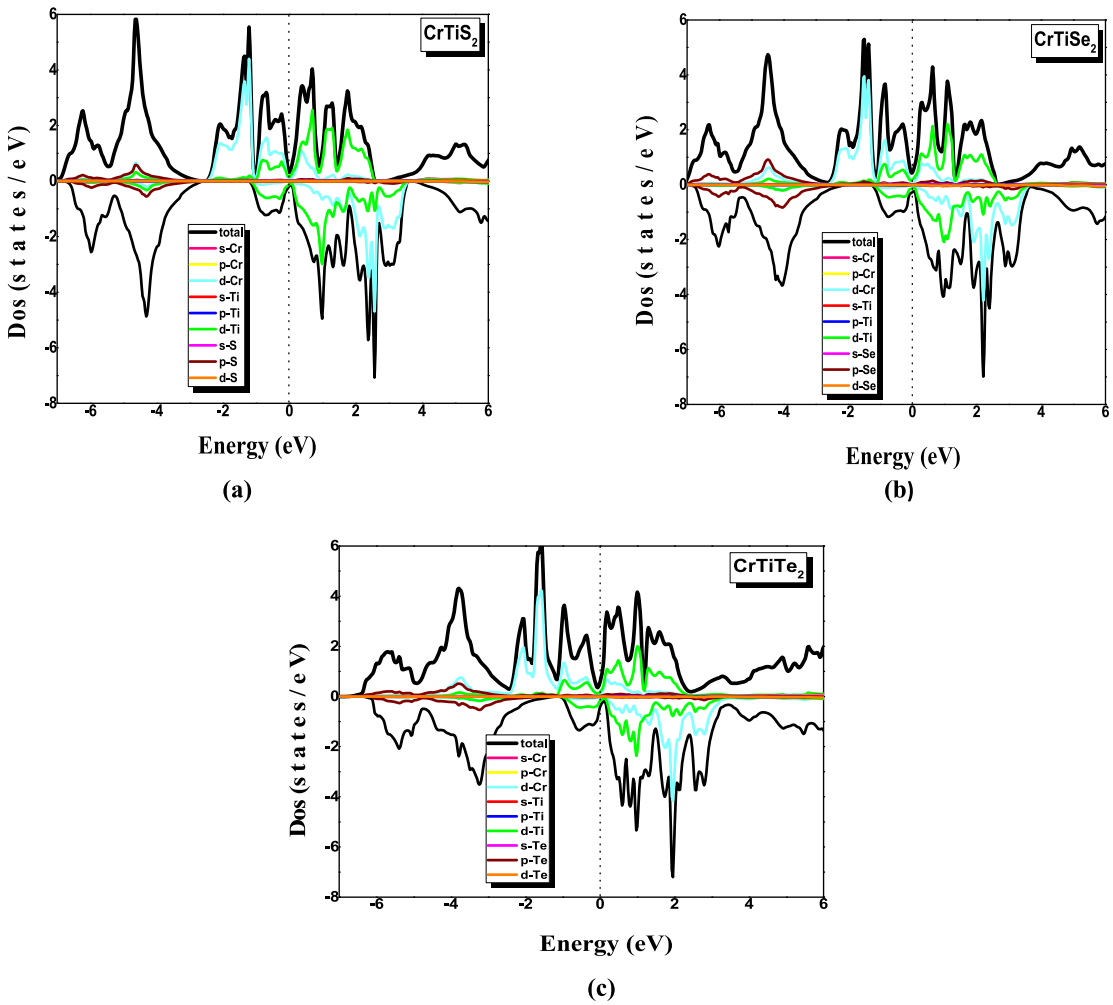

Figure 7. The calculated total and partial density of states for $CrTiX_2$(X = S,Se and Te) using EV-GGA.

moments induced on the Ti sites are a critical feature. This is particularly pronounced in the Mn- and Fe-sulfides and selenides, where the Ti moment is negative relative to the positive Y moment. This signifies a strong antiferromagnetic (AFM) coupling between the intercalant and the Ti atoms. This coupling is mediated through a superexchange-like mechanism via the intervening chalcogen (X) atoms: The Y-*d* and Ti-*d* orbitals hybridize with the X-*p* orbitals, creating a spin-dependent hopping pathway that favors an antiparallel alignment between the two metal sites. The substantial positive moment in the interstitial region (m_{int}), especially notable in the Cr-based compounds (e.g., ~1.0 μ_B~ in $CrTiTe_2$), is not an artifact but a crucial physical quantity. It represents the delocalized, itinerant spin density associated with the hybridized valence bands—primarily derived from Y-*d*, Ti-*d*, and X-*p* orbitals.

The magnetic state of Cr_xTiS_2 evolves significantly with increasing chromium concentration (x). It transitions from Pauli paramagnetism at $x = 0$, to cluster-glass behavior in the range $0.25 \leqslant x \leqslant 0.33$, and finally to antiferromagnetic order at $x = 0.5$ [45]. Similarly, in Co_xTiS_2, magnetic ordering depends on the cobalt concentration and is linked to the spatial arrangement of the Co atoms [46]. At $x = 0.20$, the compound exhibits antiferromagnetic ordering with a ferromagnetic component, though most of the sample volume remains paramagnetic. For higher concentrations ($x = 0.30$ and 0.50), a weak ferromagnetic ordering is present. Finally, $Co_{0.75}TiS_2$ is unambiguously ferromagnetic, with a Curie temperature of 370 K. The magnitude of m_{int} ~ is a direct measure of the degree of spin polarization and covalency in the system. Its increase across the chalcogen series S → Se → Te for a given intercalant correlates with increasing lattice parameter and reduced *d*-*p* hybridization strength, which allows for more localized spin density not attributed to the atomic spheres. The evolution of the total moment across the intercalant series (Cr → Mn → Fe) follows a trend that deviates from the pure ionic model. For example, the calculated moments for Cr^{3+} (d^3) are close to the spin-only value of 3 μ_B, with the excess moment arising from the positive polarization of the interstitial and host atoms. For $Mn^{2+}/^{3+}$ (d^4/d^5), the moments are reduced from the high-spin d^5 value of 5 μ_B, a signature of strong hybridization and the aforementioned AFM coupling to Ti, which quenches the net moment. The further reduction in moment

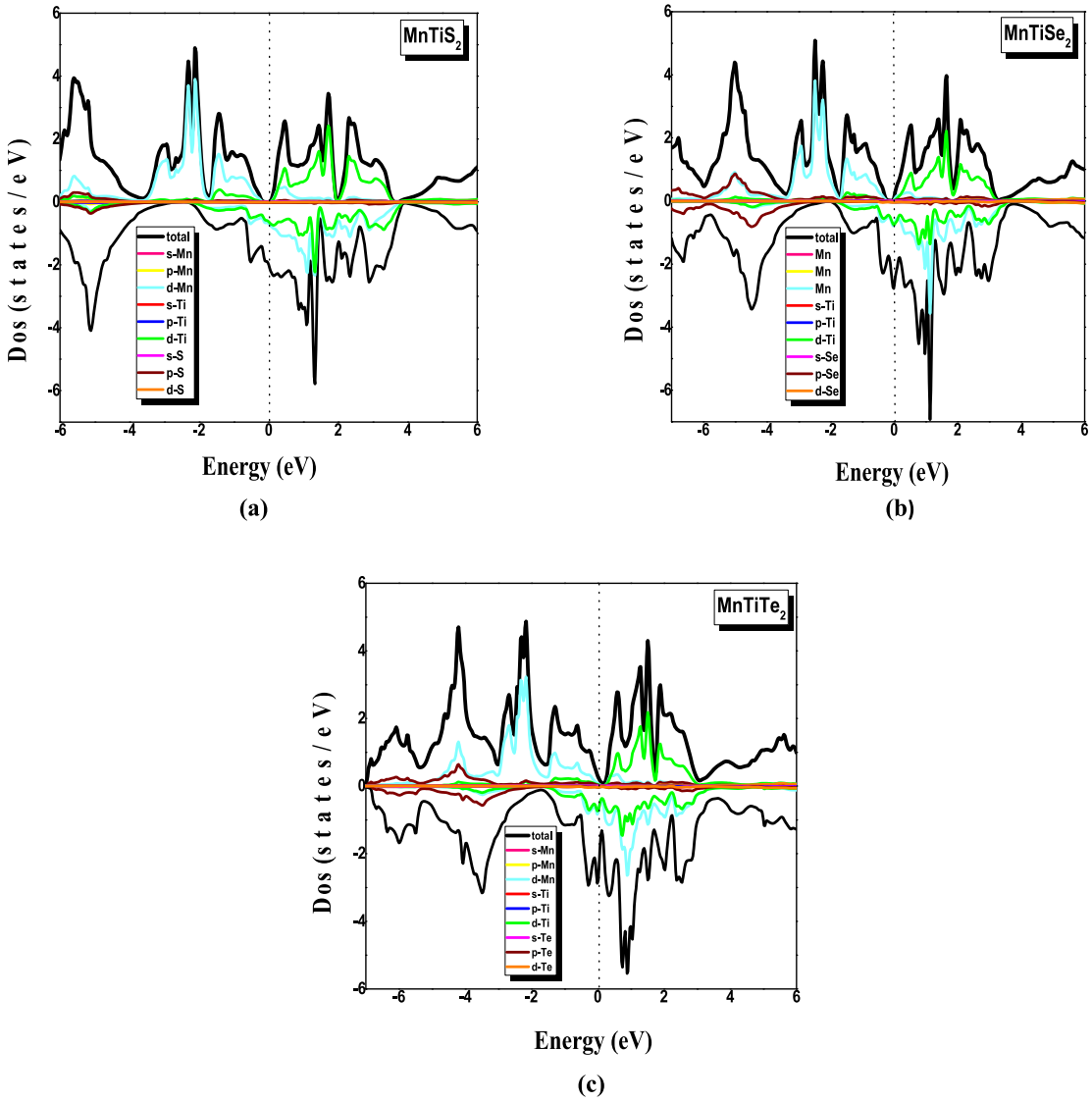

Figure 8. The calculated total and partial density of states for $MnTiX_2$(X = S, Se and Te) using EV-GGA.

for $Fe^{2+}/^{3+}$ (d^6/d^7) is consistent with a low-spin or intermediate-spin state induced by the octahedral crystal field of the chalcogen atoms and strong covalent bonding, which promotes electron delocalization and moment reduction. Intercalating titanium dichalcogenides with 3d transition metals typically localizes the material's conduction electrons [47]. However, the degree of localization and the resulting physical properties are highly sensitive to two factors: the occupancy of the impurity atom's 3d electron shell and the extent of covalent bonding involving these d electrons. The systematic variation with chalcogen atom underscores the critical role of ligand chemistry. The larger, more polarizable telluride ions enhance covalency and double-exchange mechanisms, leading to complex, non-monotonic behavior in the moment that cannot be explained by a simple ionic picture.

The magnetic moment of nickel in Ni_xTiSe_2 is believed to be itinerant [48]. A strong correlation exists between the change in the lattice parameter c_0 and the value of the effective magnetic moment; this correlation is observed in both Ni_xTiSe_2 and similar systems intercalated with other 3d metals. This suggests that the magnetic moment of the intercalant is governed by the degree of hybridization between the metal's 3d states and the electronic bands of the $TiSe_2$ host. In contrast, all Mn_xTiSe_2 compounds exhibit simple paramagnetic behavior above approximately 15 K [49].

The electronic and structural behavior predicted by our calculations for the intercalated $YTiX_2$ compounds is consistent with the broader understanding of guest–host interactions in transition metal dichalcogenides. In particular, our identified electronic structure and stability for $FeTiS_2$ are strongly supported by the recent specialized *ab initio* study of Chubarova and Mamonova on the $Fe_{1/3}TiS_2$ compound [50]. Furthermore, the covalent hybridization between the intercalant's *d*-states and the host Ti-*d* and X-*p* states, which we observe in the projected density of states and which underlies the complex magnetic interactions, aligns with the experimental

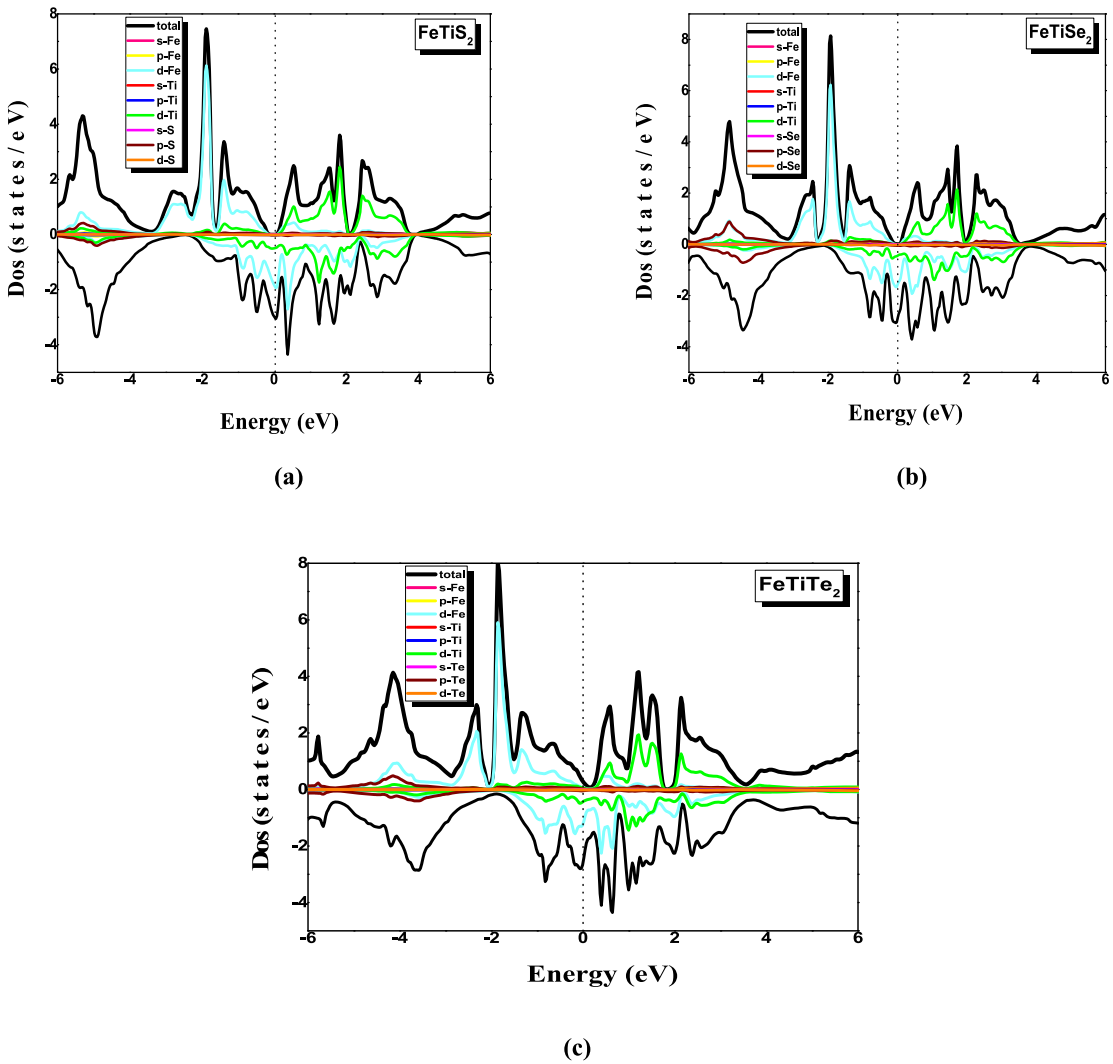

Figure 9. The calculated total and partial density of states for $FeTiX_2$(X = S, Se and Te) using EV-GGA.

Table 3. Total magnetic moment m_{tot} (μ_B), local magnetic moment per atom and magnetic moment in the interstitial region (m_{int}) in $YTiX_2$(Y = Cr, Mn and Fe, X = S, Se and Te) compounds.

Compounds	GGA					EV-GGA				
	Y(μ_B)	Ti(μ_B)	X(μ_B)	m_{int} (μ_B)	m_{tot} (μ_B)	Y(μ_B)	Ti(μ_B)	X(μ_B)	m_{int} (μ_B)	m_{tot} (μ_B)
$CrTiS_2$	2.989	0.109	0.006	0.586	3.698	3.417	0.097	−0.023	0.560	4.027
$MnTiS_2$	3.298	−0.371	0.015	0.055	3.012	3.196	−0.339	0.019	0.018	2.914
$FeTiS_2$	2.759	−0.332	0.016	−0.164	2.296	2.278	−0.244	0.036	−0.029	2.077
$CrTiSe_2$	3.128	0.185	−0.021	0.753	4.023	3.259	0.162	−0.052	0.737	4.054
$MnTiSe_2$	3.504	0.176	0.032	0.791	4.536	3.788	0.458	0.016	0.933	5.214
$FeTiSe_2$	2.107	−0.181	0.034	0.001	1.995	2.219	−0.257	0.047	−0.061	1.996
$CrTiTe_2$	2.820	0.173	−0.033	1.145	4.070	3.047	0.161	−0.065	0.995	4.073
$MnTiTe_2$	2.709	−0.098	0.005	0.319	2.942	2.980	−0.277	0.029	0.176	2.938
$FeTiTe_2$	1.448	0.082	−0.006	0.128	1.645	1.969	−0.111	0.014	0.063	1.950

and theoretical model of guest–host chemical bonding established by Shkvarin *et al* for related systems [51]. This consistency confirms that our GGA approach reliably captures the essential physics of intercalation in this material family. Furthermore, the insertion of transition-metal atoms between the layers of transition-metal dichalcogenides (TMDs) has emerged as an effective strategy for designing van der Waals (vdW) materials with tunable functionalities. Transition-metal intercalation has been reported to induce a range of novel physical phenomena in TMDs. For example, copper intercalation in $TiSe_2$ leads to superconductivity [52], while the incorporation of magnetic elements into layered TMDs can generate long-range magnetic ordering and enable

Table 4. Calculated elastic constants C_{ij} (GPa), for hexagonal phase of TiX_2(X = S, Se and Te) and $YTiX_2$ (Y = Cr, Mn and Fe , X = S, Se and Te) compounds using GGA approximations.

Compounds	C_{11}	C_{33}	C_{55}	C_{12}	C_{13}
TiS_2-NM	184.42	161.09	88.99	59.04	78.27
$CrTiS_2$-FM	155.70	182.16	86.85	32.72	55.26
$MnTiS_2$-FM	157.52	167.19	117.51	21.61	67.24
$FeTiS_2$-FM	160.84	202.60	95.09	35.84	92.78
$TiSe_2$-NM	144.23	136.11	73.38	45.70	66.85
$CrTiSe_2$-FM	126.71	140.20	73.84	28.54	52.31
$MnTiSe_2$-FM	223.47	499.96	78.09	14.72	25.71
$FeTiSe_2$-FM	127.40	129.59	78.28	21.98	94.59
$TiTe_2$-NM	102.95	103.25	58.86	34.99	49.68
$CrTiTe_2$-FM	121.43	109.35	73.22	15.81	51.89
$MnTiTe_2$-FM	119.61	121.83	104.79	27.08	92.64
$FeTiTe_2$-FM	171.64	86.50	136.77	59.50	67.44

electrical switching behavior, which are highly desirable for spintronic applications [53]. Such findings highlight the importance of exploring metal-intercalated and few-layer TMD systems to tailor their electronic, magnetic, and optical responses.

In the absence of prior experimental or theoretical studies, these results constitute a first-principles prediction of the complex magnetic state in these materials. They suggest a fascinating interplay between localized moments on the intercalants and itinerant magnetism in the host layers, pointing towards potential for non-collinear spin textures or tunable magnetic coupling in this family of van der Waals materials. Verification of these predictions, particularly the antiparallel Ti alignment, would be a key objective for future neutron scattering or spin-polarized STM experiments.

3.3. Mechanical properties and elastic tensor analysis

The second-order elastic stiffness tensor, C_{ij}, provides a fundamental description of the linear response of a crystal to applied stress and is paramount for assessing mechanical stability, bonding character, and anisotropic behavior. For a crystal with hexagonal symmetry, the tensor is characterized by five independent components: C_{11}, C_{12}, C_{13}, C_{33}, and C_{44} (where $C_{44} = C_{55}$) [54]. The computed components, presented in table 4, were validated against the necessary and sufficient Born–Huang stability criteria for a hexagonal lattice [55]:

$$C11 > |C12|, \quad C44 > 0, \quad C33 > 0, \quad (C11 + C12)\ C33 > 2C13^2 \tag{1}$$

All compounds satisfy these conditions, confirming their mechanical stability in the calculated ground-state structures.

A detailed examination of the elastic constants reveals systematic trends governed by chemical composition and structural evolution. For the pristine TiX_2 series, a monotonic reduction in the magnitude of all C_{ij} components is observed with increasing chalcogen atomic number (e.g., C_{11} diminishes from 184.4 GPa for TiS_2 to 102.9 GPa for $TiTe_2$). This softening is a direct consequence of the increasing ionic radius and metallic character of the chalcogen, which leads to longer bond lengths, reduced overlap integrals, and consequently, weaker bonding forces. Furthermore, the relationship $C_{11} > C_{33}$ for TiX_2 is indicative of the pronounced mechanical anisotropy inherent to layered van der Waals materials, where strong covalent intralayer bonding within the basal plane confers greater stiffness than the weaker interlayer interactions along the *c*-axis.

Intercalation with transition metal atoms (Y = Cr, Mn, Fe) induces a significant restructuring of the mechanical anisotropy. In many $YTiX_2$ compounds, this results in an inversion of the stiffness relationship, yielding $C_{33} > C_{11}$ (e.g., $CrTiS_2$: $C_{33} = 182.2$ GPa, $C_{11} = 155.7$ GPa; $MnTiSe_2$: $C_{33} = 500.0$ GPa, $C_{11} = 223.5$ GPa). This inversion signifies that the intercalant acts as a covalent pillar within the van der Waals gap, substantially enhancing the interlayer bonding strength and stiffness along the [001] direction. The exceptionally high C_{33} value for $MnTiSe_2$ suggests a potential coupling between its magnetic ordering and the lattice response, or the formation of particularly strong, directional hybridized bonds involving the Mn *d*-states.

The macroscopic elastic moduli—bulk modulus (B), shear modulus (G), and Young's modulus (E)—were derived from the C_{ij} components using the Voigt-Reuss-Hill (VRH) averaging scheme [56–58], which provides bounds for the actual polycrystalline values. The Hill average (B_H, G_H, E_H) of these bounds is reported in table 5, along with the Poisson's ratio (ν_H) and Pugh's ratio (B_H/G_H). The bulk modulus, which measures resistance to uniform compression, and the shear modulus, which measures resistance to shape-changing shear deformation, both decrease across the series $TiS_2 > TiSe_2 > TiTe_2$. This trend mirrors the reduction in C_{ij} and is

Table 5. Calculated bulk modulus B, shear modulus G (GPa), Young modulus E (GPa), Poisson ratio υ (GPa) and B/G for hexagonal phase of TiX_2(X = S, Se and Te) and $YTiX_2$ (Y = Cr, Mn and Fe, X = S, Se and Te) compounds using GGA approximations.

Compounds	B_v	B_R	B_H	G_V	G_R	G_H	E_V	E_R	E_H	υ_V	υ_R	υ_H	B/G
TiS_2-NM	106.79	106.78	106.78	69.09	63.98	66.54	170.50	160.00	165.28	0.23	0.25	0.24	1.60
$CrTiS_2$-FM	86.67	85.06	85.86	70.39	67.58	68.98	166.18	160.29	163.24	0.18	0.18	0.18	1.24
$MnTiS_2$-FM	78.66	67.95	73.31	89.54	67.70	78.62	194.74	152.47	173.75	0.08	0.12	0.10	0.93
$FeTiS_2$-FM	107.45	98.07	102.76	70.73	61.33	66.03	174.01	152.26	163.15	0.23	0.24	0.23	1.55
$TiSe_2$-NM	87.04	86.85	86.94	55.54	50.64	53.09	137.41	127.20	132.34	0.23	0.25	0.24	1.63
$CrTiSe_2$-FM	73.33	71.96	72.64	56.71	52.72	54.72	135.27	127.12	131.21	0.19	0.20	0.19	1.32
$MnTiSe_2$-FM	119.91	103.73	111.82	110.8	98.26	104.5	254.18	224.05	239.12	0.14	0.14	0.14	1.07
$FeTiSe_2$-FM	89.63	48.45	69.04	53.40	11.59	32.50	133.66	32.22	84.276	0.25	0.38	0.29	2.12
$TiTe_2$-NM	64.20	63.86	64.03	41.99	37.25	39.62	103.43	93.56	98.54	0.23	0.25	0.24	1.61
$CrTiTe_2$-FM	65.71	64.85	65.28	55.35	47.09	51.22	129.66	113.75	121.81	0.17	0.20	0.18	1.27
$MnTiTe_2$-FM	87.31	35.775	61.542	61.08	6.23	33.66	148.59	17.68	85.40	0.21	0.41	0.26	1.82
$FeTiTe_2$-FM	90.95	81.09	86.02	81.61	49.82	65.71	188.47	124.05	157.14	0.15	0.24	0.19	1.30

Table 6. Calculated longitudinal, transversal and average sound velocities (υ_l, υ_t, υ_m respectively, in m/s) and Debye temperature (Θ_D, in K) for TiX_2(X = S, Se and Te) and $YTiX_2$ (Y = Cr, Mn and Fe , X = S, Se and Te) compounds in hexagonal structure using GGA approximation.

Compounds	υ_l (m/s)	υ_t (m/s)	υ_m (m/s)	$\Theta_D(K)$
TiS_2-NM	7757.74	4525.79	5019.83	559.26
$CrTiS_2$-FM	6315.70	3933.49	4334.77	520.20
$MnTiS_2$-FM	6308.98	4191.34	4584.01	547.55
$FeTiS_2$-FM	6386.28	3756.91	4163.84	503.86
$TiSe_2$-NM	5486.16	3182.93	3532.14	376.82
$CrTiSe_2$-FM	4966.15	3044.38	3360.57	380.88
$MnTiSe_2$-FM	6597.47	4256.05	4671.64	523.50
$FeTiSe_2$-FM	4259.91	2290.87	2557.74	293.09
$TiTe_2$-NM	4309.72	2509.45	2783.86	277.44
$CrTiTe_2$-FM	4517.38	2797.42	3084.7	325.22
$MnTiTe_2$-FM	3739.12	2102.86	2339.77	258.69
$FeTiTe_2$-FM	4607.13	2834.26	3127.48	353.90

consistent with increasing lattice softness. Young's modulus, E_H, a measure of tensile stiffness, follows the same order, confirming TiS_2 as the most rigid compound.

The nature of chemical bonding and the propensity for ductile versus brittle fracture can be quantitatively assessed using Pugh's ratio (B_H/G_H) and Poisson's ratio (ν_H). According to Pugh's criterion [59], a B_H/G_H ratio greater than 1.75 suggests a material will exhibit ductile behavior, as the resistance to volume change (metallic bonding characteristic) dominates over resistance to shear deformation (covalent bonding characteristic). Most compounds in this study are brittle ($B_H/G_H < 1.75$), consistent with their predominant mixed ionic-covalent bonding. The notable exceptions are $FeTiSe_2$ ($B_H/G_H = 2.12$) and $MnTiTe_2$ ($B_H/G_H = 1.82$), which indicate a transition towards ductile behavior. This is likely due to enhanced metallicity from the intercalant and the more polarizable telluride and selenide ions, which facilitate charge delocalization and allow for plastic deformation via dislocation motion.

Poisson's ratio, ν, provides further insight into bonding character. For central-force solids, ν is typically 0.25; values significantly lower than this indicate strong directional covalent bonding (e.g., diamond, $\nu \approx 0.1$), while higher values ($\geqslant$0.33) are characteristic of metallic bonding [60]. The calculated ν_H values for $MnTiS_2$ (0.10) are indicative of highly directional covalent bonds. In contrast, the elevated values for $FeTiSe_2$ (0.29) and $MnTiTe_2$ (0.26) suggest a reduced directionality of bonds and a more metallic contribution to the atomic bonding, corroborating the ductility predicted by Pugh's ratio.

The longitudinal (ν_l), transverse (ν_t), and average (ν_m) sound velocities, along with the Debye temperature (Θ_D), were calculated from the elastic moduli and density, as presented in table 6. The Debye temperature, which characterizes the highest possible phonon frequency and is correlated with thermal conductivity, melting point, and hardness, decreases significantly from TiS_2 ($\Theta_D = 559$ K) to $TiTe_2$ ($\Theta_D = 277$ K). This trend is a direct result of the decreasing sound velocities, which themselves are governed by the reduction in elastic stiffness and increase in density across the series.

The significant differences between the Voigt and Reuss bounds for certain compounds (e.g., $FeTiSe_2$, $MnTiTe_2$) indicate substantial elastic anisotropy. This anisotropy can be quantified using parameters such as the Zener anisotropy factor ($A = 2C_{44}/(C_{11}–C_{12})$) for the basal plane and the ratio C_{33}/C_{11} for the *c*-axis. Such anisotropy implies that mechanical properties like stiffness and thermal expansion are highly direction-dependent, which has critical implications for device performance under mechanical stress and for microcrack propagation.

To the best of our knowledge, this work presents the first complete dataset of second-order elastic constants and derived mechanical properties for this full family of magnetic intercalates. The results provide crucial predictions for their mechanical behavior, highlighting compounds with exceptional anisotropy ($MnTiSe_2$) and potential ductility ($FeTiSe_2$, $MnTiTe_2$). These findings establish an essential foundation for future experimental validation and for the design of functional materials where mechanical integrity and anisotropic response are critical, such as in flexible spintronic devices.

The directional dependence of the elastic moduli provides a definitive visual representation of the mechanical anisotropy inherent in these crystalline systems. For a perfectly isotropic material, the three-dimensional surface depicting a modulus such as Young's modulus (E) would form a perfect sphere, indicating identical mechanical response in all crystallographic directions [61–64]. The pronounced deviations from spherical symmetry observed in the three-dimensional surfaces of Young's modulus for all compounds, as shown in figure 11, constitute direct and unambiguous evidence of significant elastic anisotropy. The morphology of

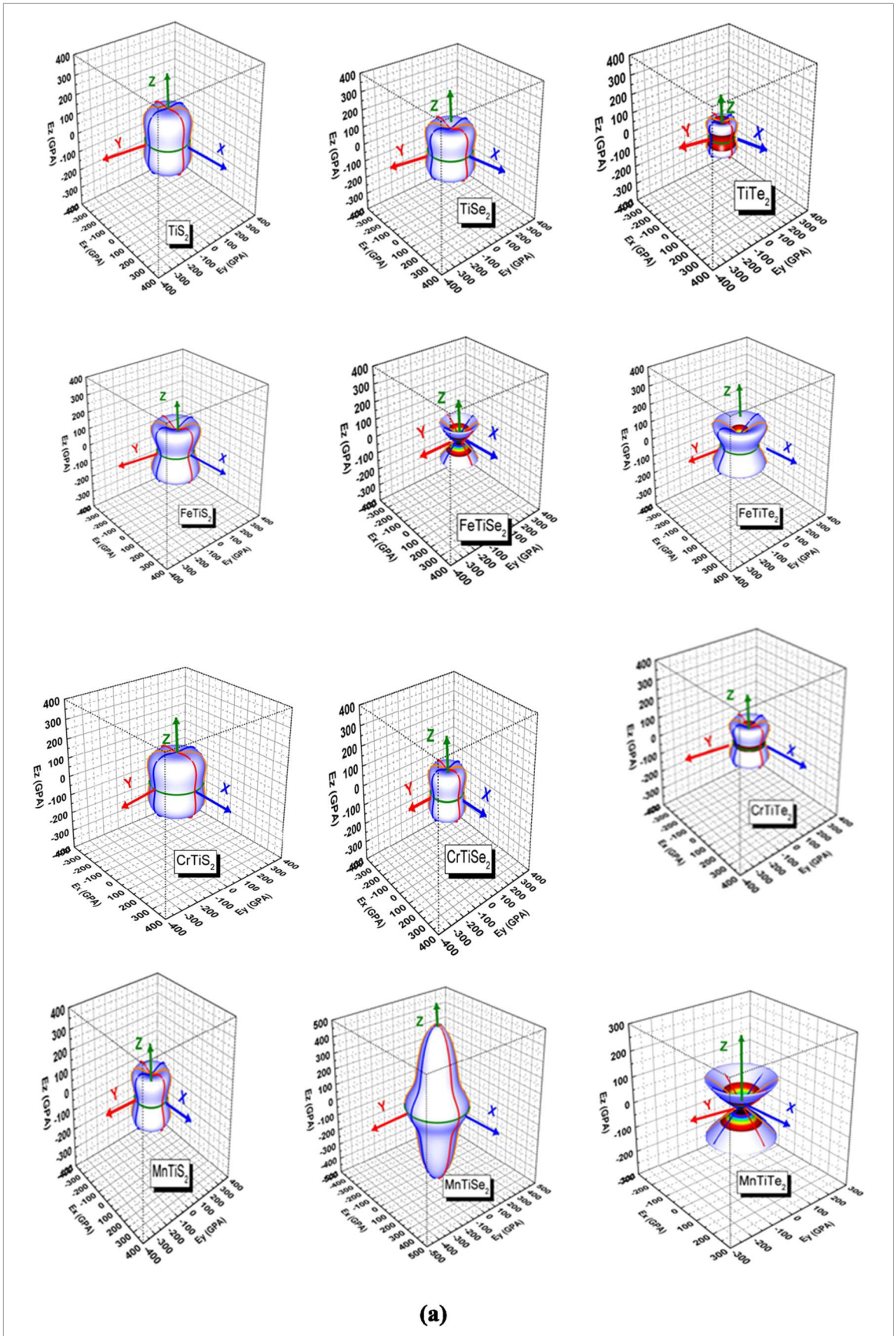

Figure 10. Graphs of (a) the 3D surface of the Young's modulus, (b) their transverse sections in separated planes, respectively.

these surfaces reveals critical structure–property relationships: the pristine TiX_2 compounds exhibit an oblate spheroidal shape, flattened along the crystallographic *c*-axis, which is the characteristic signature of layered van der Waals materials where strong covalent intralayer bonding confers high in-plane stiffness while weak

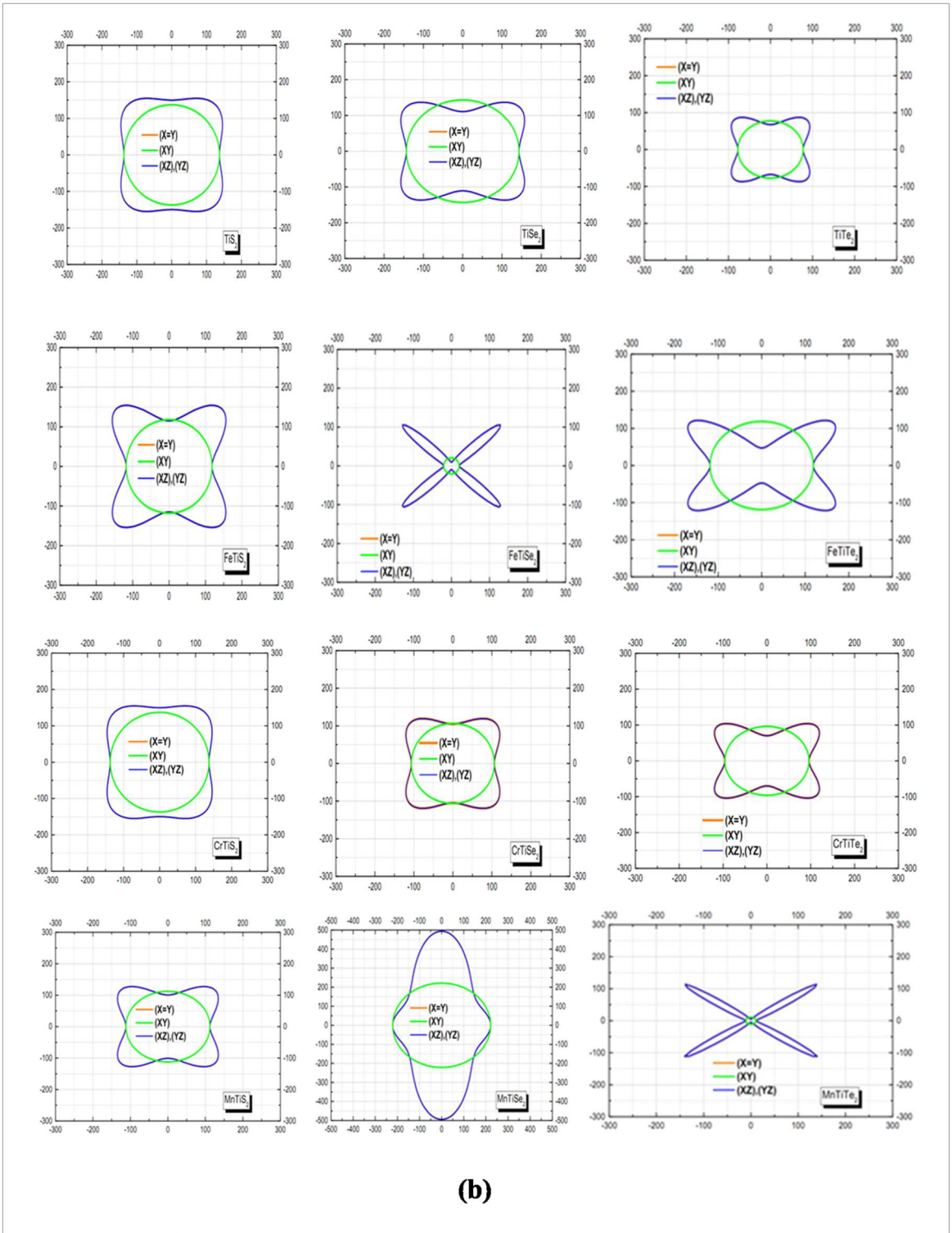

Figure 10. (Continued.)

interlayer interactions result in lower out-of-plane stiffness. In contrast, the $YTiX_2$ intercalates display a marked evolution in surface geometry, with many compounds—particularly those such as $CrTiS_2$ and $MnTiSe_2$—showing a distinct bulging along the *c*-axis approaching a prolate spheroidal form. This transformation visually encapsulates the mechanistic pillar effect of intercalation, whereby the guest atoms enhance covalent bonding along the [001] direction, thereby increasing the C_{33} elastic constant and fundamentally altering the mechanical anisotropy from the parent compound.

The two-dimensional transverse sections provide quantitative insight into the anisotropy within specific crystallographic planes. The contours within the basal plane are nearly circular for all compounds, confirming the expected in-plane isotropy consistent with the hexagonal symmetry. However, the sections through prismatic planes reveal profound asymmetry, vividly illustrating the stark contrast between the in-plane ([100]) and out-of-plane ([001]) stiffness. The elongation along the in-plane axes and contraction along the *c*-axis for

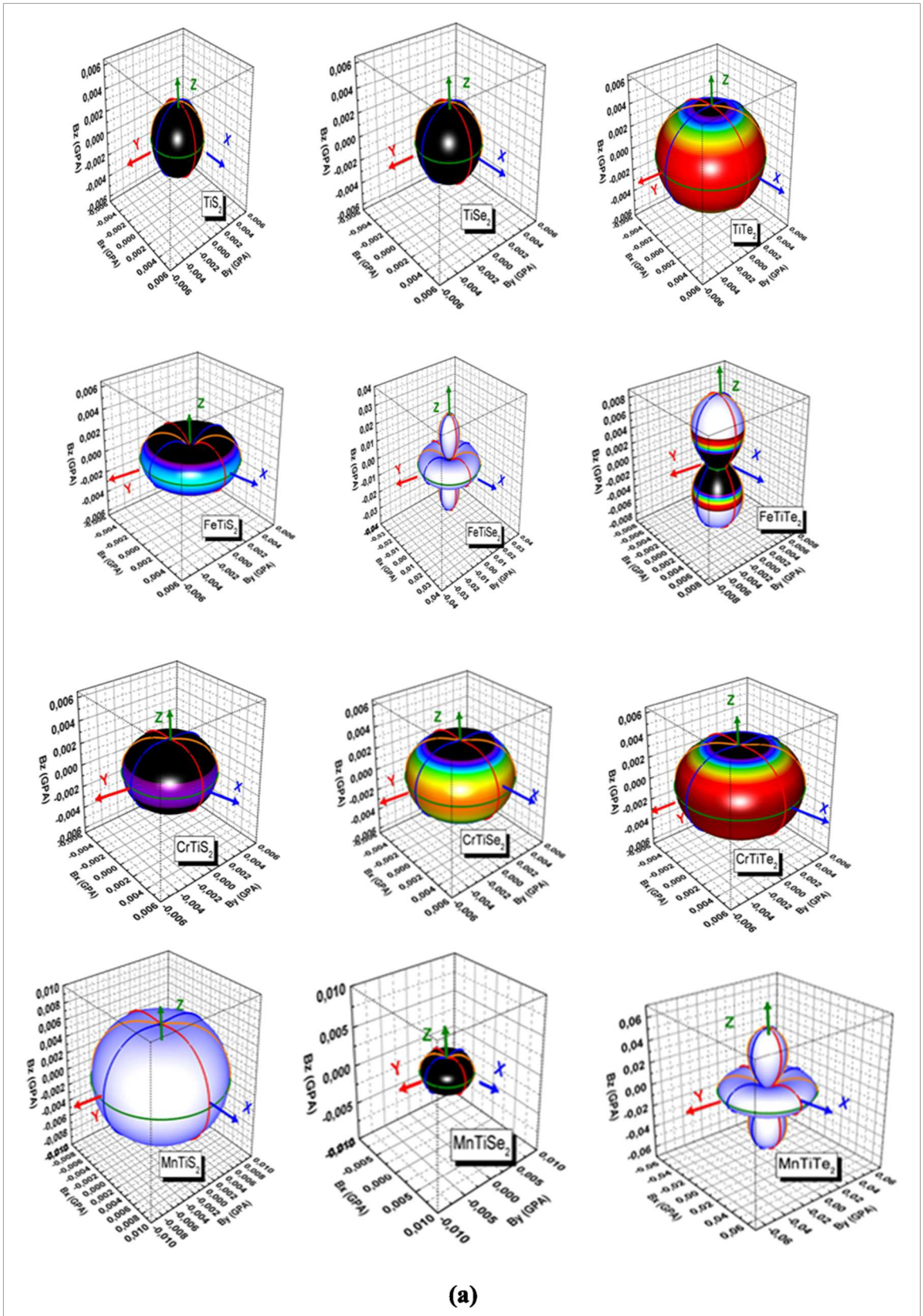

Figure 11. Graphs of (a) the 3D surface of the bulk modulus, (b) their transverse sections in separated planes, respectively.

TiX_2 visually corroborates the relationship $C_{11} > C_{33}$, whereas the more balanced or even inverted profiles for the intercalated compounds reflect the trend where $C_{33} > C_{11}$ becomes prevalent.

The directional dependence of the bulk modulus (B), presented in figure 11, offers a complementary perspective. The three-dimensional surfaces for B are notably closer to spherical than those for E, as the bulk modulus, representing resistance to uniform compression, is generally less sensitive to directional variations

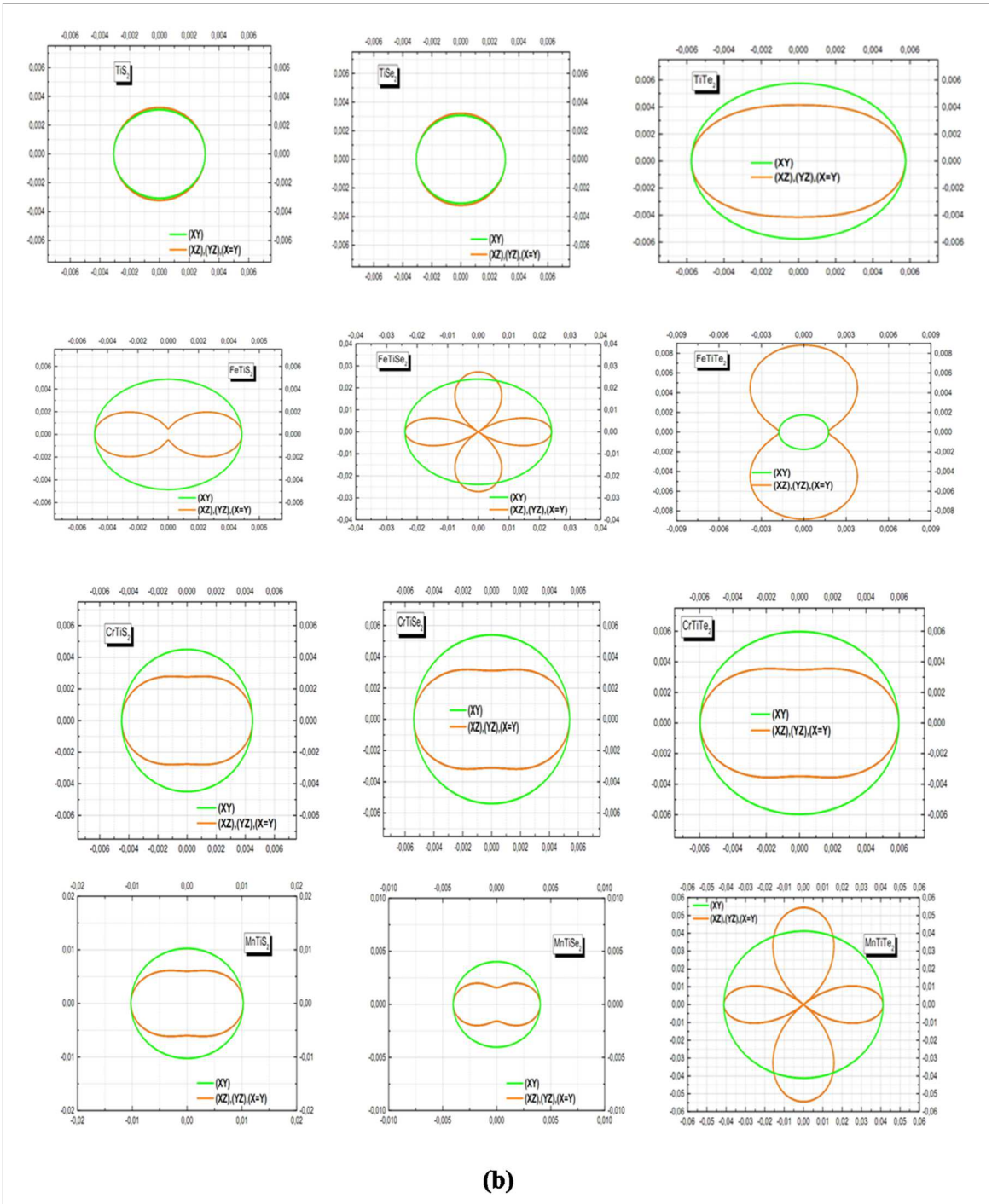

Figure 11. (Continued.)

than the shear-dependent Young's modulus. Nevertheless, the observable deviations from perfect sphericity remain physically significant. The slight elliptical distortion observed for the TiX_2 series, with minor compression along the *c*-axis, indicates that hydrostatic compression is marginally easier normal to the layers, directly reflecting the compressibility of the van der Waals gap. For the intercalated compounds, the surfaces exhibit increased asphericity, particularly for systems like $MnTiSe_2$ with its exceptionally high C_{33} value. This confirms that intercalation introduces a measurable anisotropy in compressibility, meaning the volumetric response to applied pressure is itself direction-dependent, a phenomenon linked to the specific values of the C_{13} elastic constant and the evolving nature of the chemical bonds.

The two-dimensional sections for the bulk modulus further quantify this behavior, showing near-perfect circular contours in the basal plane but clear elliptical distortions in the prismatic planes. This contrast graphically illustrates the isotropic compressibility within the layers against the anisotropic compressibility across them. In summary, the visualizations in figures 10 and 11 provide a powerful geometric confirmation of the anisotropic mechanical behavior deduced from the calculated elastic constants. They transcend numerical

tables by illustrating how the mechanical properties are not intrinsic scalars but are fundamentally direction-dependent tensorial properties. The evolution of the Young's modulus surface from a disk-like shape for TiX_2 to a more complex morphology for $YTiX_2$ offers a direct visual correlation to the structural modification induced by intercalation. This level of anisotropy is a critical consideration for any potential device application, as the mechanical response—including stiffness, fracture propensity, and thermal expansion—will be inherently dependent on the crystallographic orientation relative to the direction of applied stress or thin-film growth.

The thermodynamic and mechanical stability predicted here for the $YTiX_2$ compounds aligns with established experimental and computational literature on intercalated TMDCs. For instance, the formation of stable superlattices and long-range ordering upon intercalation is a well-documented phenomenon, as reviewed by Wang *et al* [65]. Prior first-principles studies on specific compounds such as $CrTiS_2$ and $MnTiS_2$ have confirmed their structural stability through lattice optimization and electronic property analysis [66, 67]. Furthermore, experimental investigations of $MTiS_2$ (M = Cr, Mn, Fe) systems have demonstrated robust structural integrity and stable charge transfer behavior post-intercalation [68]. These reports, together with our calculated equilibrium structural parameters and satisfaction of the Born–Huang mechanical stability criteria, consistently affirm that the $YTiX_2$ structures investigated in this work are thermodynamically and mechanically stable, and are plausible candidates for synthesis via established routes such as molten-salt intercalation [69].

4. Conclusions

We have conducted a comprehensive first-principles investigation into the structural, electronic, magnetic, and mechanical properties of TiX_2 and their intercalated derivatives $YTiX_2$. Our findings reveal that the lattice parameters of these materials align well with existing data and follow predictable chemical trends, with the lattice expanding systematically upon intercalation. The guest atoms serve to separate the chalcogen layers, promoting structural changes.

The electronic properties undergo significant transformation, transitioning from semiconducting to metallic or half-metallic states with intercalation. Notably, compounds like $MnTiS_2$ and $FeTiS_2$ exhibit half-metallic ferromagnetism with 100% spin polarization, positioning them as key candidates for spin-filtering applications. The magnetic ground state is complex, involving localized moments on the intercalants and anti-parallel induced moments on the Ti atoms, a manifestation of the strong antiferromagnetic superexchange coupling facilitated by the chalcogen atoms.

Mechanically, the compounds maintain stability and exhibit notable elastic anisotropy, with intercalation altering their mechanical responses. The intercalation often results in a stiffening along the *c*-axis and reverses the anisotropy, which is visually confirmed through 3D and 2D modulus visualizations. While most materials are brittle, $FeTiSe_2$ and $MnTiTe_2$ stand out with predicted ductile behavior, suggesting greater damage tolerance.

This study presents a thorough theoretical foundation for understanding these magnetic intercalates, offering detailed insight into their half-metallicity, tunable magnetic coupling, and anisotropic mechanical properties. These characteristics highlight their potential for applications in spintronic devices.

Moreover, the weak van der Waals bonding between the chalcogen layers in these bulk structures implies that they can be readily exfoliated into few-layer or monolayer forms without disrupting the intrinsic in-plane bonding framework. This opens an exciting opportunity to explore 2D metal-intercalated TiX_2 systems, where reduced dimensionality may further enhance quantum confinement, magnetic exchange coupling, and spin polarization effects. Previous studies have already shown that monolayer TiS_2 transitions from semimetallic to semiconducting behavior upon exfoliation, suggesting that analogous effects could modulate the electronic and magnetic responses of intercalated analogues. Therefore, $YTiX_2$ monolayers and few-layer systems are expected to retain or even amplify their half-metallic ferromagnetism, making them promising candidates for 2D spintronic and magneto-optoelectronic applications.

Our results thus pave the way for future experimental research, including the synthesis and characterization of 2D monolayers and few-layer intercalated TiX_2 systems, guiding the technological exploration of these promising layered materials. Finally, while our study provides a comprehensive foundation, the use of standard DFT functionals means that the van der Waals interactions between layers are not explicitly captured. Future work employing vdW-corrected functionals (e.g., DFT-D3 or vdW-DF) would be valuable to obtain more precise interlayer spacings and binding energies, which is particularly important for understanding properties like exfoliation energy and interlayer shear mechanics.

Acknowledgments

The authors (Dj. Guendouz, T. Ghellab, Z. Charifi and H. Baaziz) would like to thank the general directorate for scientific research and technological development for their financial support during the realization of this work.

Data availability statement

All data that support the findings of this study are included within the article (and any supplementary files).

Author contributions

Dj Guendouz
Conceptualization (lead), Data curation (lead), Software (lead), Writing – review & editing (lead)

H Baaziz 0000-0003-4860-2740
Conceptualization (lead), Investigation (supporting), Writing – original draft (Equal), Writing – review & editing (lead)

T Ghellab
Investigation (lead), Methodology (lead), Validation (lead), Writing – review & editing (lead)

Z Charifi 0000-0003-3875-4716
Formal analysis (lead), Supervision (lead), Validation (lead), Writing – original draft (supporting), Writing – review & editing (lead)

References

[1] Friend R H and Yoffe A D 1987 *Adv. Phys.* **36** 1
[2] Progress in Intercalation Research 1994 ed W MullerWarmuth and R Schollhorn (Kluwer Academic)
[3] Hassan M Z and Kane C L 2010 *Rev. Mod. Phys.* **82** 3045
[4] Anderson O, Karschnick G, Manzke R and Skibowski M 1985 *Solid State Commun.* **53** 339
[5] Rasch J C E, Stemmler T, Müller B, Dudy L and Manzke R 2008 *Phys. Rev. Lett.* **101** 237602
[6] Kidd T E, Miller T, Chou M Y and Chiang T-C 2002 *Phys. Rev. Lett.* **88** 226402
[7] Doni E and Girlanda R 1986 *Electronic Structure and Electronic Transitions in Layered Materials* ed V Grasso (Reidel)
[8] Chen C H, Fabian W, Brown F C, Woo K C, Davies B and de Long B 1980 *Phys. Rev. B* **21** 615
[9] Bachrach R Z, Skibowski M and Brown F C 1976 *Phys. Rev. Lett.* **37** 40
[10] Drube G, Karschnik M, Skibowski R, Thies and Volkert K 1980 *Proc. of the 15th Int. Conf. on the Physics of Semiconductors (Kyoto)* edited by S Tanaka and Y Toyozawa [J. Phys. Soc. Jpn. Suppl. A 49 (1980}] 137
[11] Traum M M, Margaritondo G, Smith N V, Rowe J E and Di Salvo F J 1978 *Phys. Rev. B* **17** 1836
[12] Friend R H, Jerome D, Liang W Y, Mikkelsen J C and Yoffe A D 1977 *J. Phys. C* **10** L705
[13] Klipstein P C and Friend R H 1982 *EurophysicsConferenceAbstracts* ed V Heine European Physical Society, Petit-Lancy 2, Switzerland Vol 6A, 351
[14] Zunger A and Freeman A J 1977 *Phys. Rev. B* **16** 906
Zunger A and Freeman A J 1978 *Phys. Rev. B* **17** 1839
[15] de Boer D K G, van Bruggen C F, Bus G W, Coehoorn R, Haas C, Sawatzky G A, Myron H W, Norman D and Padmore H 1984 *Phys. Rev. B* **29** 6797
[16] Krusius P, von Boehm J and Isoma¨ki H 1975 *J. Phys.* **C8** 3788
[17] Andersen O K 1975 *Phys. Rev. B* **12** 3060
[18] Singwi K S, Sjo¨lander A, Tosi M P and Land R H 1970 *Phys. Rev. B* **1** 1044
[19] Isoma¨ki H, von Boehm J and Krusius P 1979 *J. Phys.* **C12** 3239
[20] Urmigar C, Ellis D E, Wang D S, Krakauer H and Posternak M 1982 *Phys. Rev.* **B26** 4935
[21] Wu Z Y, Lemoigno F, Gressier P, Ouvrard G, Moreau P, Rouxel J and Natoli C R 1996 *Phys. Rev.* **B54** R11009
[22] von Boehm J and Isomaki H M 1981 *J. Phys. C* **14** L-75
[23] Clerc D G, Poshusta R D and Hess A C 1996 *J. Chem. Phys.* **100** 15735
[24] Fang C M, de Groot R A and Haas C 1997 *Phys. Rev. B* **56** 4455
[25] Allan D R, Kelsey A A, Clark S J, Angel R J and Ackland G J 1998 *Phys. Rev. B* **57** 5106
[26] Liu B, Yang J, Liu C, Hu T, Han Y and Gao C 2011 *Phy. Statu. Solidi* **C8** 1683–6
[27] Guller F, Helman C and Llois A M 2012 *Physica B* **407** 3188–91
[28] Shkvarin A S, Yarmoshenko Y M, Skorikov N A, Yablonskikh M V, Merentsov A I, Shkvarina E G and Titov A N 2012 *J. Exp. The. Phy.* **114** 150–6
[29] Shkvarin S, Merentsov A I, Shkvarina E G, Yarmoshenko Y M, Pis I, Nappini S and Titov A N 2018 *J. Chem. Phy.* **148** 124707
[30] Rajaji V, Dutta U, Sreeparvathy P C, Sarma S C, Sorb Y A, Joseph B, Sahoo S, Peter S C, Kanchana V and Narayana C 2018 *Phy. Rev. B* **97** 085107
[31] Kim Y-S, Li J, Tanaka I, Koyama Y and Adachi H 2000 *Mat. Trans. Jim.* **41** 1088–91

[32] Matssushita T, Suga S and Kimuta A 1999 *Phys. Rev. B* **60** 1678–86
[33] Ueda Y, Negishi H, Koyana M and Inoue M 1986 *Solid State Comm.* **57** 839–42
[34] Perdew J P, Ruzsinszky A, Csonka G I, Vydrov O A, Scuseria G E, Constantin L A, Zhou X and Burke K 2008 *Phys. Rev. Lett.* **100** 136406
[35] Parmar V B and Vora A M 2021 *East Eur. J. Phys.* **1** 93–8
[36] Parmar V B and Vora A M 2022 *BIBECHANA* **19** 97–101
[37] Blaha P, Schwarz K, Madsen G K H, Kvasnicka D, Luitz J, Computer code Wien2K; improved and updated Unix version of the original, Blaha P, Schwarz K, Sorantin P and Rickey S B 1990 *Comput. Phys. Commun.* **59** 399
[38] Perdew J P, Burke K and Ernzerhof M 1996 *Phys. Rev. Lett.* **77** 3865
[39] Engel E and Vosko S H 1993 *Phys. Rev. B* **47** 13164
[40] Murnaghan F D 1944 *Proc. Natl. Acad. Sci. U.S.A.* **30** 244
[41] Goodenough J B 1967 *Colloque CNRS no157 Or- say 1965* 263
[42] Arnaud Y and Chevreton M 1981 *J. Solid State Chem.* **39** 230
[43] McCanny J V 1979 *J. Phys. C: Solid State Phys.* **12** 3263
[44] Haidry A A, Ghani F, Fatima Q, Usmani M K, Ali Q, Raza A, Sajjad M and Naz G 2024 *Mater. Today Commun.* **41** 110601
[45] Pleschov V G, Baranov N V, Titov A N, Inoue K, Bartashevich M I and Goto T 2001 *J. of Alloys and Compounds* **320** 13–7
[46] Urusovaa N V, Merentsov A I, Stepanova E A and Reznitskikha O G 2023 *Chalcogenide Letters* **20** 343–51
[47] Kuranov A V, Pleshchev V G, Titov A N, Baranov N V and Krasavin L S 2000 *Phys. Solid State* **42**
[48] Baranov N V, Inoue K, Maksimov V I, Ovchinnikov A S, Pleschov V G, Podlesnyak A, NTitov A and Toporova N V 2004 *J. Phys. Condens. Matter* **16** 9243–58
[49] Maksimova V I, Baranova N V, Pleschov V G and Inoue K 2004 *J. Alloys Compd.* **384** 33–8
[50] Chubarova A A and Mamonova M V 2024 *Acad. Sci. Phys.* **88** 1415–22
[51] Shkvarin A S, Yarmoshenko Y M, Merentsov A I, Píš I, Bondino F, Shkvarina E G and Titov A N 2018 *Chemistry* **57** 5544–53
[52] Morosan E, Zandbergen H W, Dennis B S, Bos J W G, Onose Y, Klimczuk T, Ramirez A P, Ong N P and Cava R J 2006 *Nat. Phys.* **2** 544–50
[53] Nair N L, Maniv E, John C, Doyle S, Orenstein J and Analytis J G 2020 *Nat. Mater.* **19** 153–7
[54] Kittel C 1996 Physique de L'état Solide, 7 ^{éme} ed
[55] Born M and Huang K 1956 *Dynamical Theory of Crystal Lattices* (Clarendon)
[56] Voigt W 1928 *Lehrbuch der Kristallphysik* (B G Teubner)
[57] Reuss A 1929 Berechnung der fließgrenze von mischkristallen auf grund der plastizitätsbedingung für einkristalle *Z. für Angew. Math. und Mech.* **9** 49–58
[58] Hill R 1952 The elastic behaviour of a crystalline aggregate, 1952 *Proc. Phys. Soc. A* **65** 349
[59] Pagh S F 1954 *Philos. Mag.* **45** 823
[60] Haines J, Léger J and Bocquillon G 2001 *Annu. Rev. Mater. Res.* **31** 1
[61] Baaziz H *et al* 2022 *J. Supercond. Nov. Magn.* **35** 1173–82
[62] Ammi H, Charifi Z, Baaziz H, Ghellab T, Bouhdjer L, Adalla S, Ocak H Y, Uğur Ş and Uğur G 2024 **87** 966–84
[63] Ghellab T, Baaziz H, Charifi Z, Latelli H, Ahmad M J A, Telfah M, Alsaad A, Telfah A, Hergenröder R and Sabirianov R 2022 *J. Magn. Magn. Mater.* **546** 168919
[64] Bensehil I *et al* 2025 *J. Supercond. Nov. Magn.* **38** 59
[65] Wang Z, Li R, Su C and Loh K P 2020 *SmartMat* **1** e1013
[66] Parmar V B and Vora A M 2021 *Eurasian Journal of Physics and Functional Materials* **5** 116–25
[67] Parmar V B and Vora A M 2022 *Sri Lankan Journal of Physics* **23** 16–26
[68] Sharma Y, Shukla S, Dwivedi S and Sharma R 2015 *Advanced Materials Letters* **6** 294–300
[69] Gao L, Li M, Hu B and Huang Q 2024 *Small* **20** 2304281